NATIONAL AERONAUTICS AND SPACE ADMINISTRATION

Technical Report 32-1349

A Mariner Orbiter Autopilot Design

E. H. Kopf

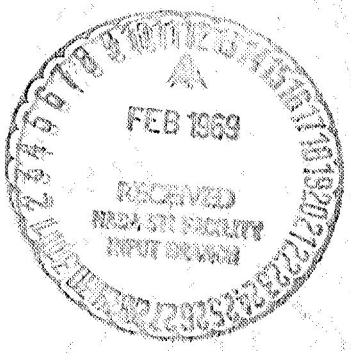

JET PROPULSION LABORATORY
CALIFORNIA INSTITUTE OF TECHNOLOGY
PASADENA, CALIFORNIA

January 15, 1969

NATIONAL AERONAUTICS AND SPACE ADMINISTRATION

Technical Report 32-1349

A Mariner Orbiter Autopilot Design

E. H. Kopf

JET PROPULSION LABORATORY
CALIFORNIA INSTITUTE OF TECHNOLOGY
PASADENA, CALIFORNIA

January 15, 1969

TECHNICAL REPORT 32-1349

Prepared Under Contract No. NAS 7-100
National Aeronautics and Space Administration

Preface

The work described in this report was performed by the Guidance and Control Division of the Jet Propulsion Laboratory.

Acknowledgment

The author wishes to acknowledge the assistance of R. F. Rathcke and R. A. Crawford of the Spacecraft Control Section for making available, sometimes through special tests, the gyroscope data used in this report.

Contents

Contents (contd)

Tables

Contents (contd)

Figures

Contents (contd)

Figures (contd)

Abstract

An autopilot for a *Mariner* orbiter, together with its design parameters, is presented. Autopilot design problems are defined, and the interfaces between the autopilot and spacecraft configuration and systems are described.

A *Mariner* Orbiter Autopilot Design

I. Introduction

This report presents a design for a thrust vector control system (autopilot) for a Mars-orbiting *Mariner* spacecraft. The spacecraft configuration considered is basically a *Mariner* Mars 1969 modified with a 300-lb-thrust gimballed engine and four propellant tanks. Since a two-tank configuration is becoming more likely for this type of mission, the effect of this change is considered in the appendices.

II. System Description and Performance Summary

A. System Description

The spacecraft configuration considered in this report and sketched in Fig. 1 shows the long-duration Rocketdyne RS-14 engine[1] pointing down the negative Z axis. The basic parameters assumed for the spacecraft and engine are presented in Tables 1 and 2.

The function of the spacecraft autopilot system is to maintain attitude control during the firing of the engine both for the long-orbit insertion burn and for the short-orbit trim and midcourse maneuvers. This is accomplished by mounting the engine in a gimbal system as

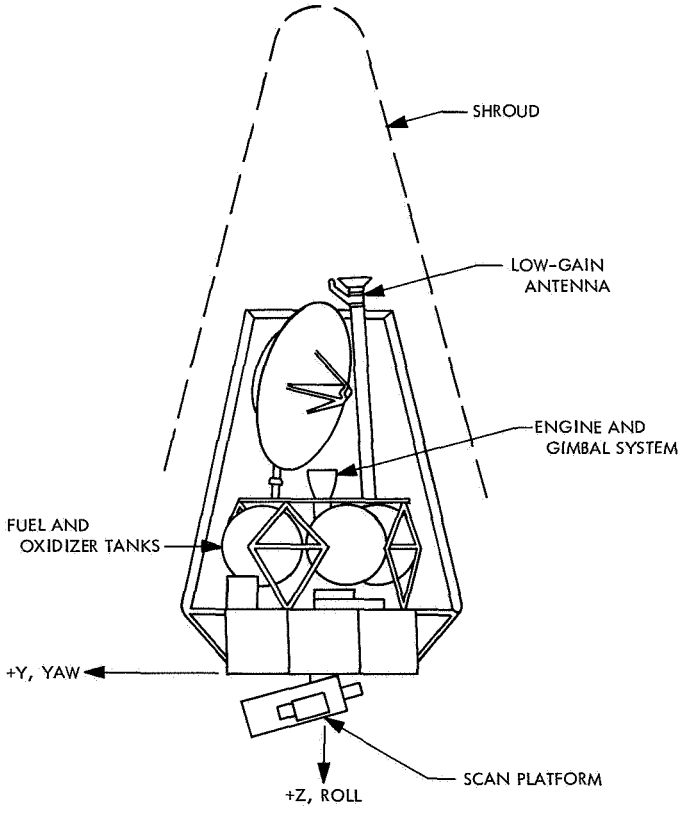

Fig. 1. *Mariner* orbiter configuration

[1]Rocketdyne, a Division of North-American Rockwell Corp.

Table 1. Spacecraft parameters

Parameter	Before orbit insertion	After insertion
Weight, lb	2043	1135
Moments of inertia, slug ft^2	I_{xx} = 278.5 I_{yy} = 291.5 I_{zz} = 365.3	233.3 237.5 304.5
CG Location, ft	X = −0.038 Y = −0.041 Z = −1.67	−0.070 −0.073 −0.923

Table 2. Engine and gimbal parameters

Parameter	Value
Nominal thrust	300 lb
Time constant	0.01 s
Weight	23 lb
Moment of inertia	0.08 slug ft^2
Swirl torque, max	2.0 in.-lb
Gimbal location, spacecraft Z axis	−3.88 ft
Gimbal deflection	±4.5 deg

shown in Fig. 2. Pointing the engine thrust vector is accomplished by two linear actuators. The gimbal actuators extend and retract a few tenths of an inch, rotating the engine in its gimbal system. It is planned that the maximum angular excursion about either gimbal axis will be ±4.5 deg. This engine rotation capability allows the autopilot system to point the thrust vector through the spacecraft center of mass and maintain attitude stability in pitch and yaw. With only this system, control cannot be effected about the spacecraft Z axis and, since swirl in the exhaust gases will produce some torque, there must be an additional control system available for roll stability. Fortunately, the needed torque can be provided by the cold-gas roll-attitude-control channel.

The autopilot system operation can be best understood by following a typical velocity change maneuver and by referring to Fig. 3. The sequence starts with CC&S event M-1, which, in preparation for the commanded turns, starts the gyros and begins the capacitor cycling. At this time the autopilot system is energized. All autopilot power could come from the present regulator which for *Mariner* Mars 1969 provides power to the jet vane autopilot. This is possible because the power required only totals 1.5 W for the pitch and yaw autopilots and approximately 6 W for the actuator servo electronics. Each actuator motor will require 20 W for a 300-ms period at turn-on and then settle down to about 7 W as the spacecraft limit-cycles under gas system control.

The commanded turns are now performed and, unlike the present jet vane actuators, the engine gimbal actuators will not experience large excursions during these turns; for example, at the deadband limit for the gas system of 3 mrad the gimbal angle is only 0.17 deg. After completion of the turns the spacecraft is oriented so that the engine is in proper inertial attitude for the velocity change maneuver. At the signal for motor ignition, the motor burn switch makes two changes in the autopilot and attitude control system. First, the cold-gas-system deadbands are increased in pitch and yaw from ±3 to ±100 mrad; this is done to prevent the wasting of large amounts of N_2 during the burn. Then, the path guidance circuits in the autopilots are enabled, and provide compensation for CG-alignment error and migration during the burn. These changes are completed simultaneously with motor ignition.

In contrast with the previous *Mariner* monopropellant engines, the bipropellant RS-14 engine builds up thrust rapidly, reaching 90% full thrust in only 20 ms. This acceleration step causes the major transient condition the autopilot system has to control. This transient arises from the resulting solar-panel hinge bending. The panels bend until they are restrained by the springs in the cruise dampers; with 300 lb of thrust this flexure can have a steady-state value of several degrees. If the panels on opposite sides of an axis are not closely matched in their hinge-bending modes, large differential torques appear

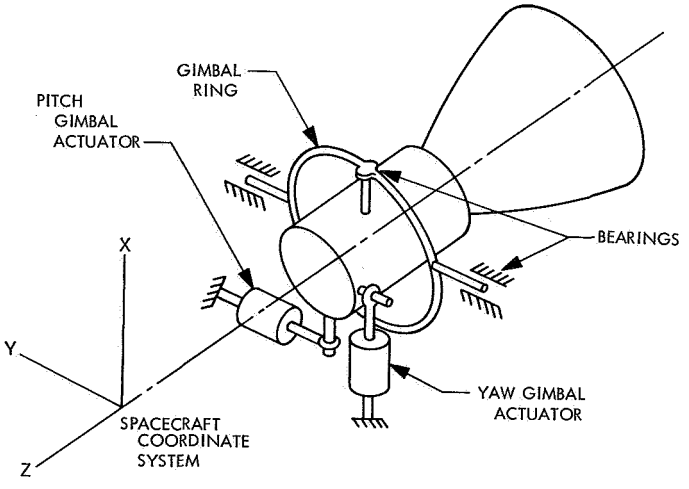

Fig. 2. Engine and gimbal sketch

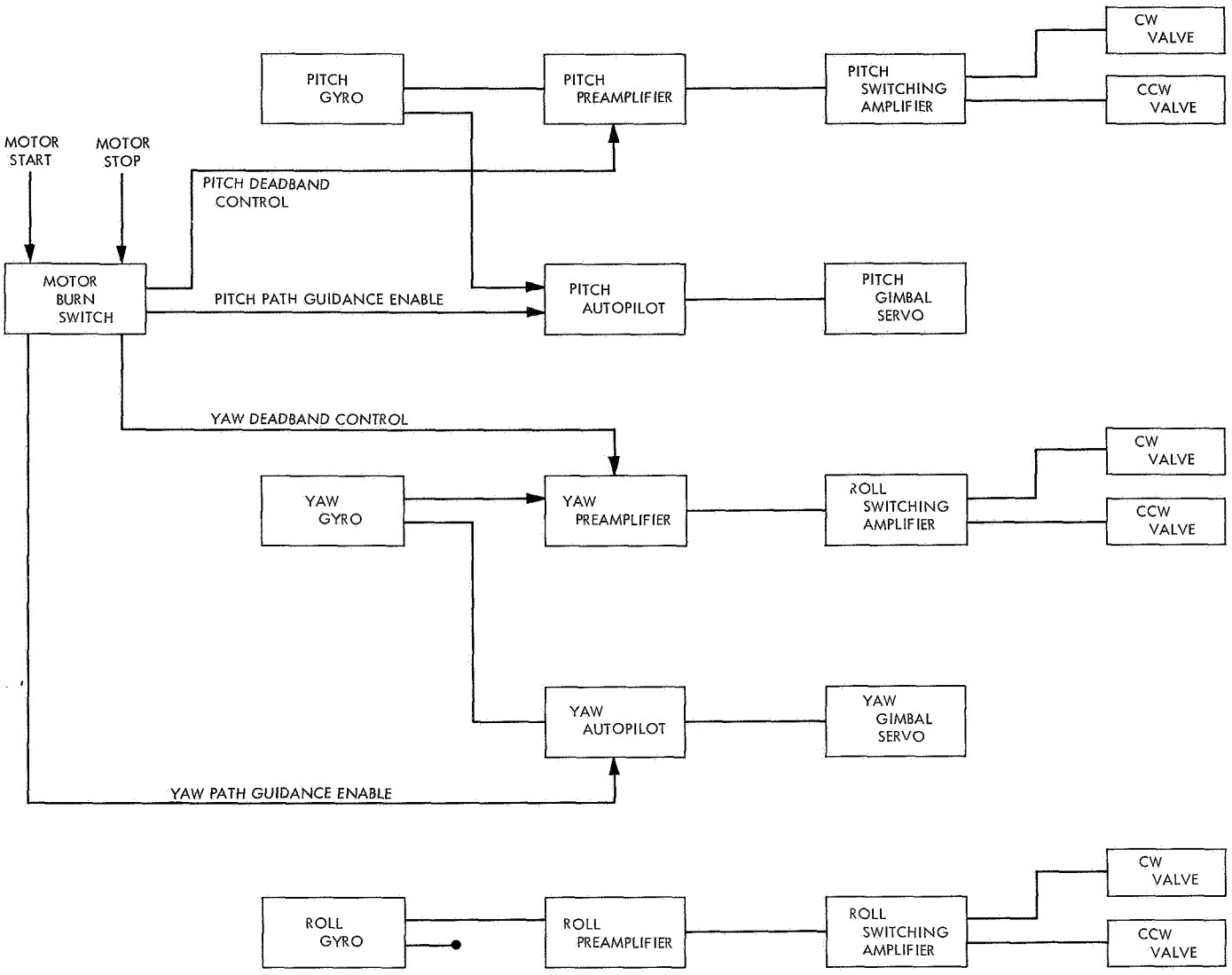

Fig. 3. *Mariner* orbiter autopilot system block diagram

on the spacecraft and, although these torques are oscillatory and do not cause position storage problems, the induced peak body rates can saturate the gyro rebalance amplifiers. During this start transient, the autopilot is in operation but the gimbal servos are essentially too slow to provide much effective control. Since gyro saturation is extremely undesirable, the design of the panel/damper system and the gimbal actuators will have to be carefully controlled.

The operation of the autopilot system during the burn is straightforward. The design of an autopilot module is shown in Fig. 4. This module receives the gyro output and feeds it to the gimbal servo. It consists of a forward path which controls the transient portion of the response and a path guidance feedback which is used to reduce steady-state error. The forward path is a 1/9-s first-order filter and controlled saturation. The filter serves two purposes: (1) gyro noise is greatly attenuated before being fed to the servo, and (2) the possibility of autopilot interaction with the unlatched scan-platform dynamics is eliminated. The controlled saturation is to prevent the gimbal servo actuator from ever being driven into its mechanical stops. The gimbal servo has a scale factor of 1/3 deg/V and mechanical stops at ± 4.5 deg.

At motor ignition the spacecraft is in the position shown in Fig. 5. After commanded turns have been performed, except for turn errors, the spacecraft Z axis is aligned with the vector **r**, the inertial reference direction for the Δv increment. The gimbal actuators are at null,

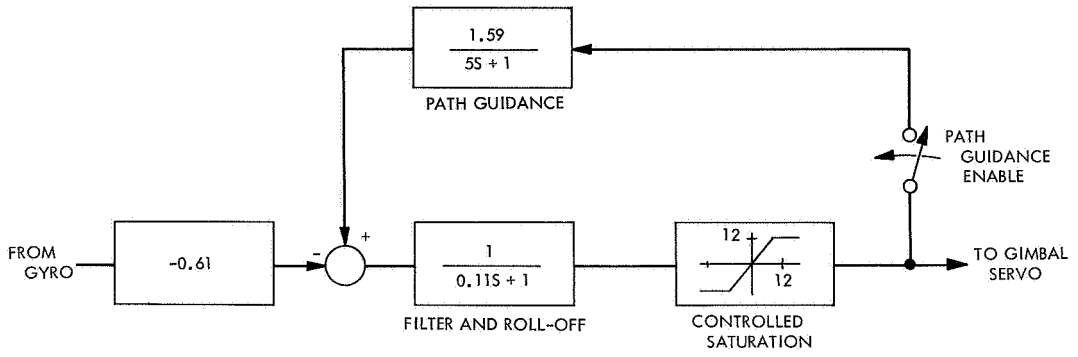

Fig. 4. *Mariner* orbiter autopilot block diagram

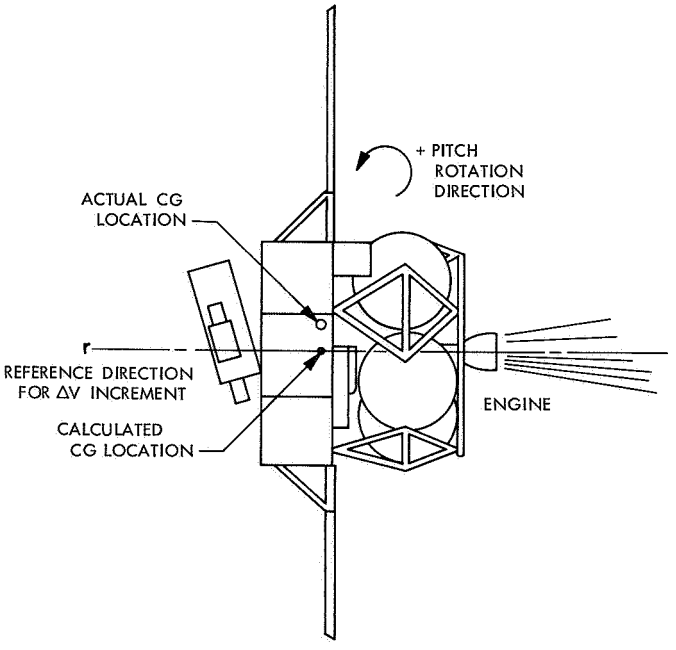

Fig. 5. Spacecraft attitude at motor ignition

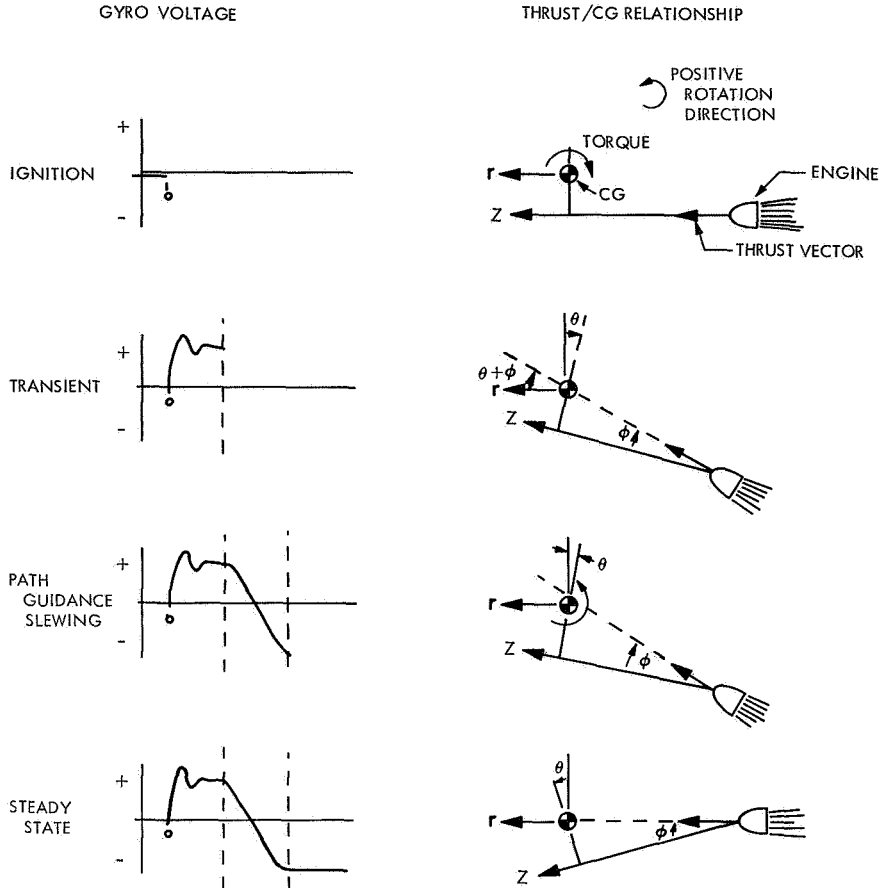

Fig. 6. Autopilot system operation

or slightly off null due to gas system limit cycling, and the engine is aligned with the calculated position of the CG. For the case under consideration, this calculated position does not coincide with the actual CG location. The evolution of the thrust-CG relationship during the burn is shown in Fig. 6. The conditions at ignition are shown in Fig. 5 and these, in turn, are duplicated in the top sketch in Fig. 6. The thrust vector is shown in the proper reference direction but misaligned with the CG. This produces a negative torque on the spacecraft and the resulting transient is shown in the second diagram in Fig. 6.

As the torque rotates the spacecraft in a negative pitch, the pitch gyro senses the error θ between the reference direction r and the Z axis, producing a positive output voltage. This voltage is filtered by the autopilot and is used to drive the gimbal servo. The engine is now rotated until the angle ϕ is sufficient to pass the thrust vector through the CG. At this time the thrust vector pointing error is $\theta + \phi$. Without path guidance the spacecraft would maintain this attitude during the entire burn, but here the path guidance amplifier, shown in Fig. 7, senses the gimbal command voltage and feeds it back to the autopilot input through a 5-s time constant. Since the command voltage is equal to the angle ϕ divided by the gimbal-servo scale factor, the positive feedback causes the angle ϕ to increase very slowly in magnitude as the time constant changes. The result on the spacecraft is a positive torque which slews the attitude. The gains in the path-guidance loop are set so that when the gyro error signal exactly cancels the positive feedback, the attitude of the spacecraft is such that thrust vector is aligned with the desired reference vector r.

Even though there is positive feedback in the path-guidance minor loop, the overall stability of the autopilot is not affected.

Engine shutdown will occur when the linear accelerometer indicates that the required Δv magnitude has been reached. At this point, the motor burn switch disables path guidance and restores the normal pitch and yaw deadbands. The removal of thrust causes the solar

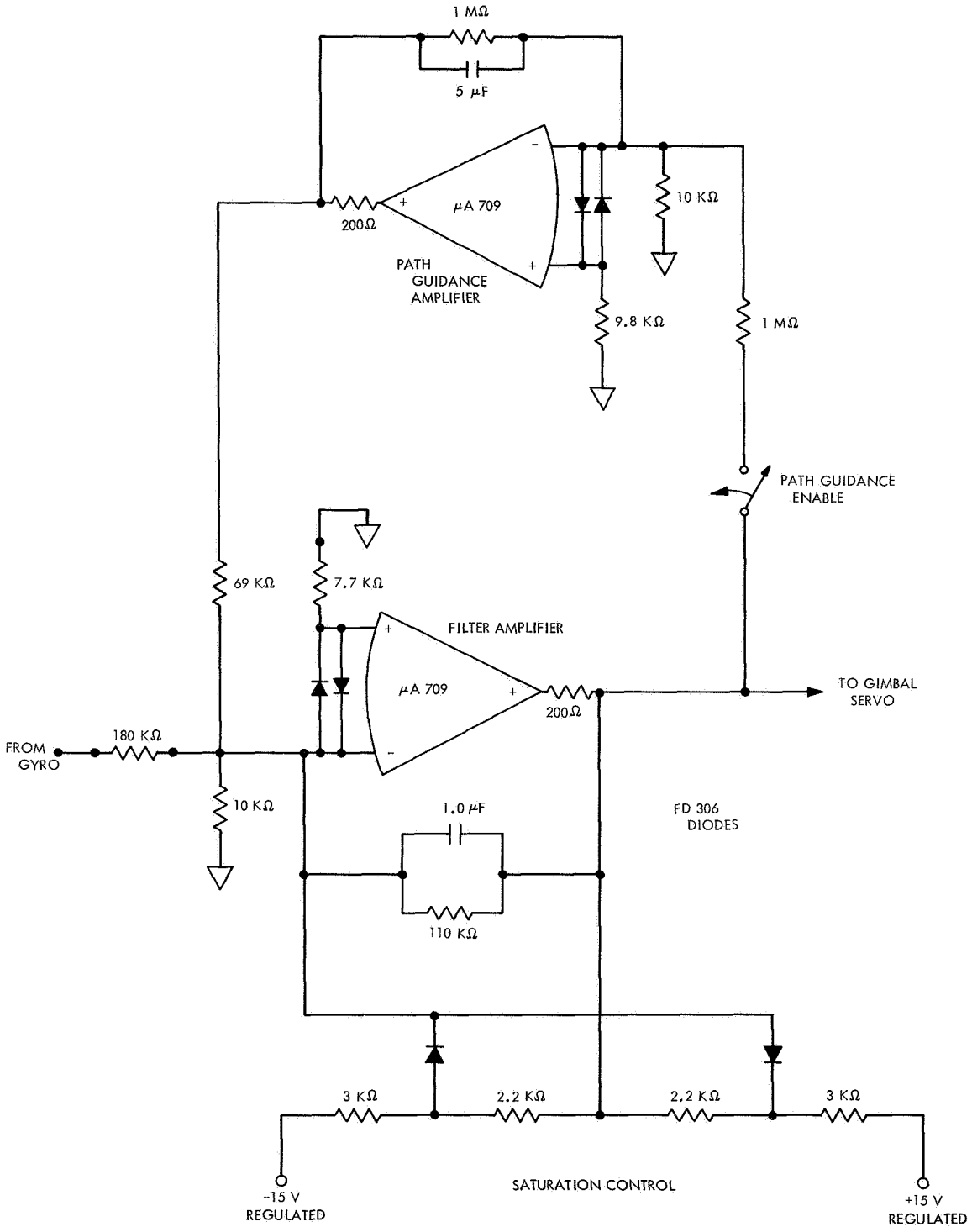

Fig. 7. Possible *Mariner* orbiter autopilot mechanization

panels to unload and another attitude transient is produced; this will be controlled by the cold-gas system, which is completely adequate for the task.

B. Performance

1. Accuracy. The accuracy of the autopilot is not defined by the thrust-vector pointing accuracy directly but in terms of the angular error from reference of the resulting Δv increment. In the following discussion of autopilot accuracy, the errors in performing the commanded turns will not be included nor will the gravity losses be considered. The autopilot error is composed of three terms:

(1) Steady-state error.

(2) Transient error.

(3) Drift error.

The important geometric parameters which contribute to these errors are shown in Fig. 8 and their values are given in Table 3.

Table 3. Autopilot error component

Symbol	Definition	Value
α_D	Gyro drift rate	0.2 deg/h, 3 σ
δ_{CG}	CG migration	0.6 in., max
δ_E	Engine position error	0.1 in., max
α_T	Actual thrust-to-engine geometric axis alignment	0.5 deg, max
α_E	Engine mounting angular error	0.5 deg, max
ΔK_G	Gyro position scale error	5.5%, 3 σ
ΔK_A	Gimbal actuator linearity	0.1 deg, 3 σ
$\Delta\phi$	Gimbal actuator resolution	0.14 deg, max

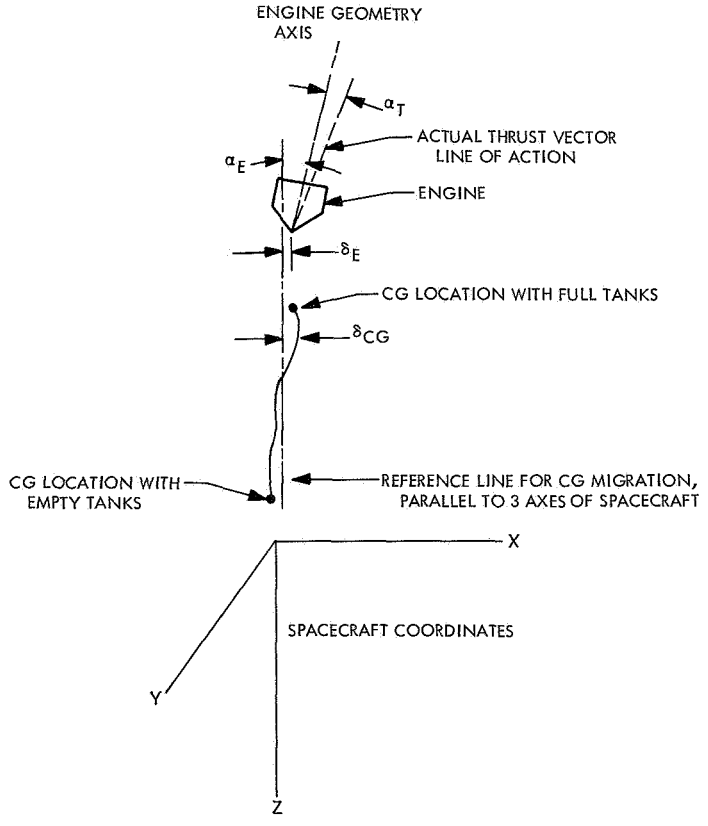

δ_{CG} = CG MIGRATION

δ_E = ENGINE MOUNTING POSITION ERROR

α_E = ENGINE MOUNTING ANGULAR ERROR

α_T = ACTUAL THRUST-TO-ENGINE GEOMETRIC AXIS ANGULAR ERROR

Fig. 8. Engine/CG relationship

Consider these errors on the single-axis basis shown in Fig. 9. Here,

δ_1 = total linear CG offset.

d_1 = distance from gimbal point to CG.

With these definitions, the total per-axis CG offset is

$$\delta = \delta_1 + d_1 (\alpha_E + \alpha_T)$$

with α_E and α_T in radians.

The equation for γ_s, the steady-state component of autopilot Δv error, is

$$\gamma_s = \alpha_T + \alpha_E + C_1 \left(\frac{\gamma_1}{d_1} \right)$$

where C_1 is dependent on gains and gain accuracy within the system and is estimated at 0.1 (worst case) and 0.063 (3 σ).

The transient error is given in Fig. 10 as a function of impulse imparted by the engine. In this plot the error angle, γ_T, has been normalized by total CG offset δ.

In part, this error is produced by solar-panel mismatch, and for this curve the panels are assumed matched to 10%. The structure enters into the transient response of the autopilot system, and the assumed parameters are given in Tables 4 and 5.

The last component is γ_D which is caused by gyro drift. If a constant drift rate k_D is assumed, the error for burn time T is

$$\gamma_D = \frac{1}{2} k_D T$$

with k_D equal to 0.2 deg/hr worst case.

2. Gimbal Servo. These actuator systems usually consist of a dc motor powering an acme screw in a hermetically sealed case; a typical system is shown in Fig. 11. This particular actuator will not have adequate force for the RS 1401, and the Autonetics actuator[2] specifically designed for this engine has too large a travel and poor resolution. At present it is hoped that a new pulse-width modulated driving servo and some gain and compensation changes will make this actuator usable.

[2]Autonetics, a Division of North-American Rockwell Corp.

Table 4. Solar panel parameters

Parameter	Value
Distance from Z axis to panel CG	6.66 ft
Distance from Z axis to panel hinge	3.12 ft
Panel moment of inertia	3.07 slug ft^2
Panel rigid bending mode frequency[a]	1 Hz, min
Panel damping[a]	0.3 to 0.7

[a]Panel rigid bending modes matched to 10% on opposite panels.

Table 5. Unlatched scan platform parameters

Parameter	Value
Spacecraft Z axis location of scan CG	0.534 ft
Spacecraft Y axis location of scan CG	0.361 ft
Spacecraft Y axis location of scan cone axis	−0.333 ft
Spacecraft Z axis location of scan cone axis	0.174 ft
Clock axis moment of inertia	5.16 slug ft^2
Cone axis moment of inertia	6.27 slug ft^2
Cone axis natural frequency	3.6 Hz
Clock axis natural frequency	3.9 Hz
Cone and clock damping	0.01
Weight	180 lb

3. Typical performance characteristics. Pitch, yaw, and roll gyro outputs for an orbit trim are shown in Fig. 12, 13, and 14. The initial thrust–CG offset is essentially along the X spacecraft axis and shows up in the yaw gyro output. The magnitude of the offset is 1.6 deg. The burn starts at 2 s.

III. System Equations and Models

A. Gyroscope Dynamics

The gain of an integrating-type gyro is the ratio of the angular momentum to the viscous damping, represented by H/D. This gain means that if the gyro is rotated through an angle θ about its input axis the gimbal will rotate as $(H/D)\ \theta$, unless it is electrically restrained by its torquing system. For spacecraft autopilots both low-gain ($H/D \approx 0.4$) and high-gain ($H/D \approx 250$) gyros can be used. *Mariner* and *Ranger* vehicles have always used high-gain gyros in closed-loop configurations. The *Mariner* gyro loop in the inertial position mode is shown in Fig. 15.

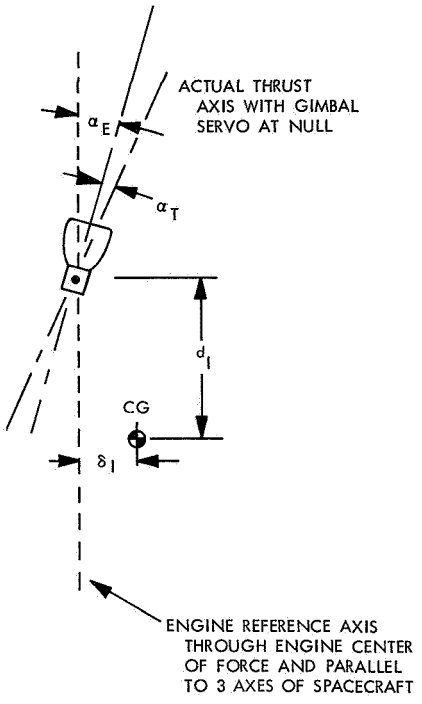

Fig. 9. Engine geometric axis with gimbal servo at null

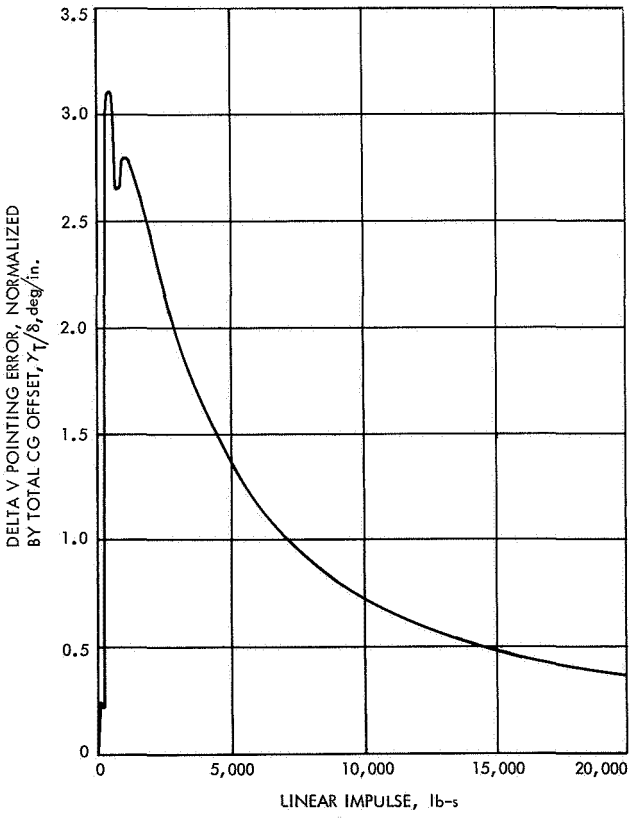

Fig. 10. Autopilot transient error

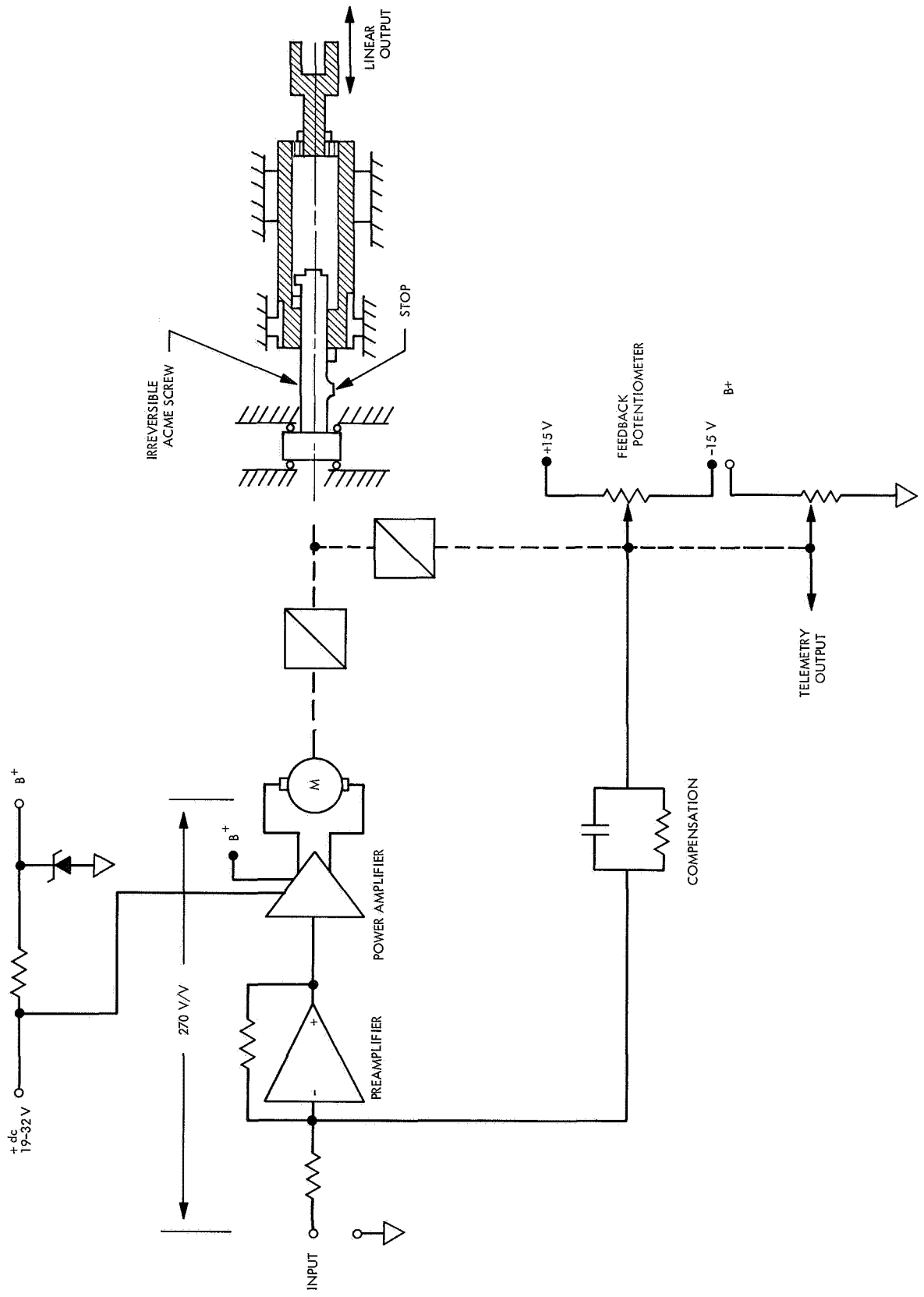

Fig. 11. *Lunar Orbiter* gimbal actuator and servo loop

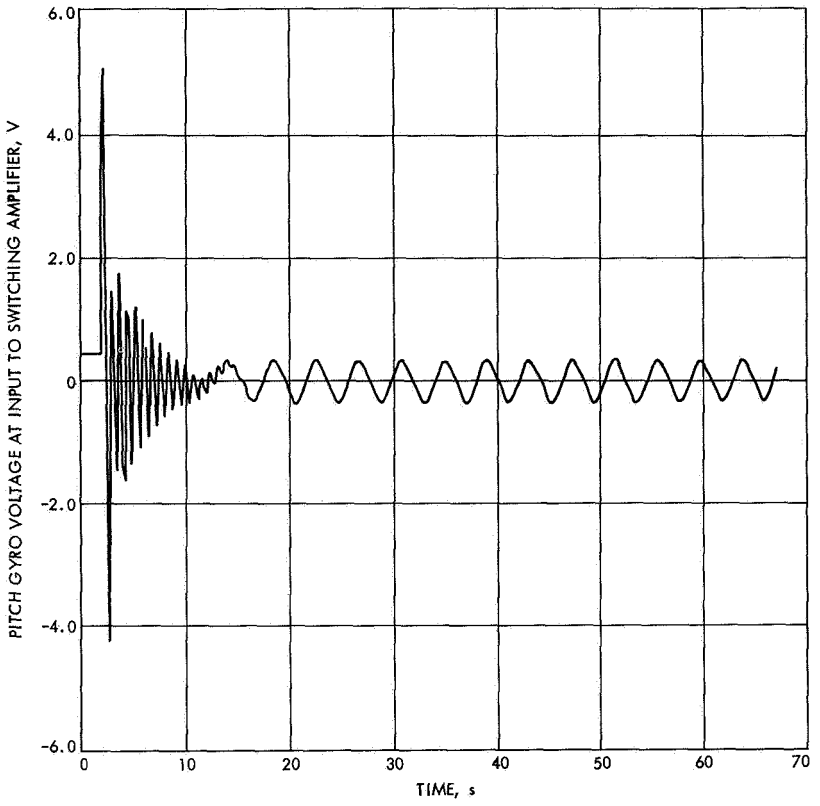

Fig. 12. Pitch gyro voltage at input to switching amplifier

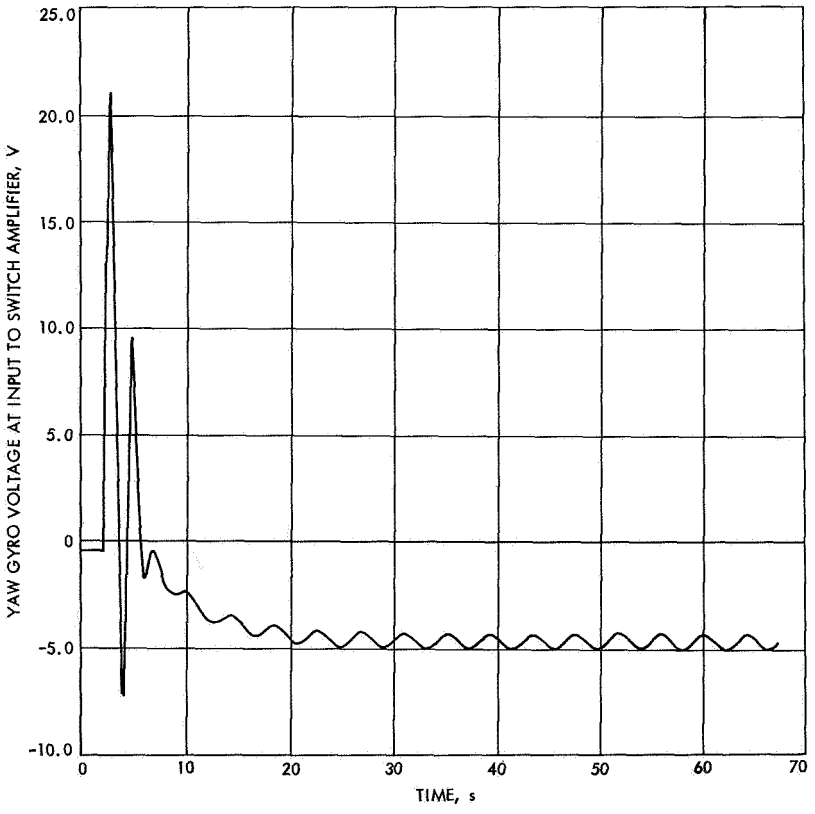

Fig. 13. Yaw gyro voltage at input to switching amplifier

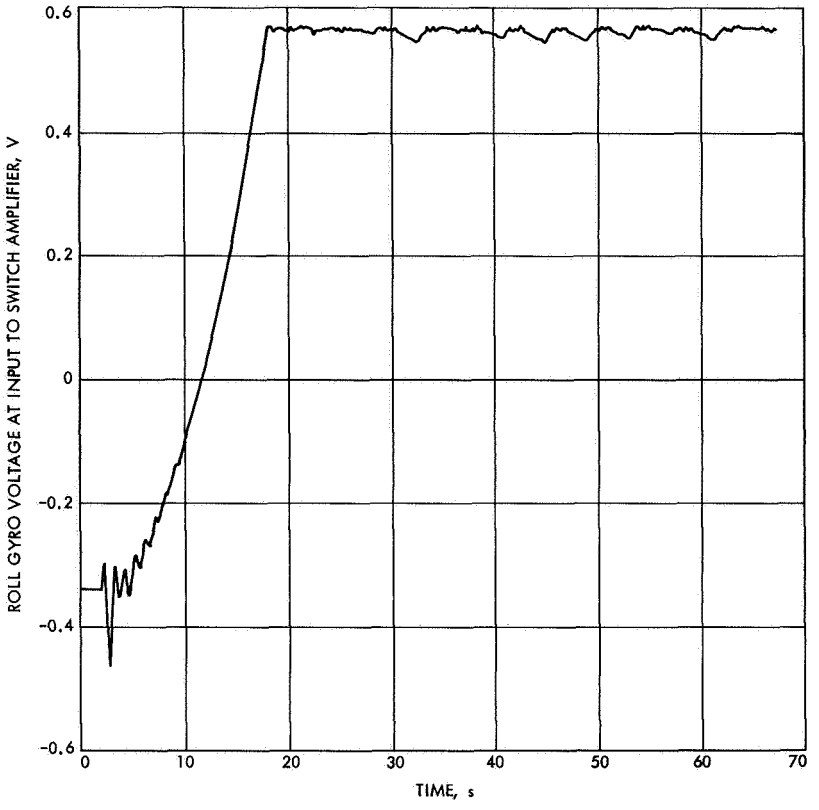

Fig. 14. Roll gyro voltage at input to switching amplifier

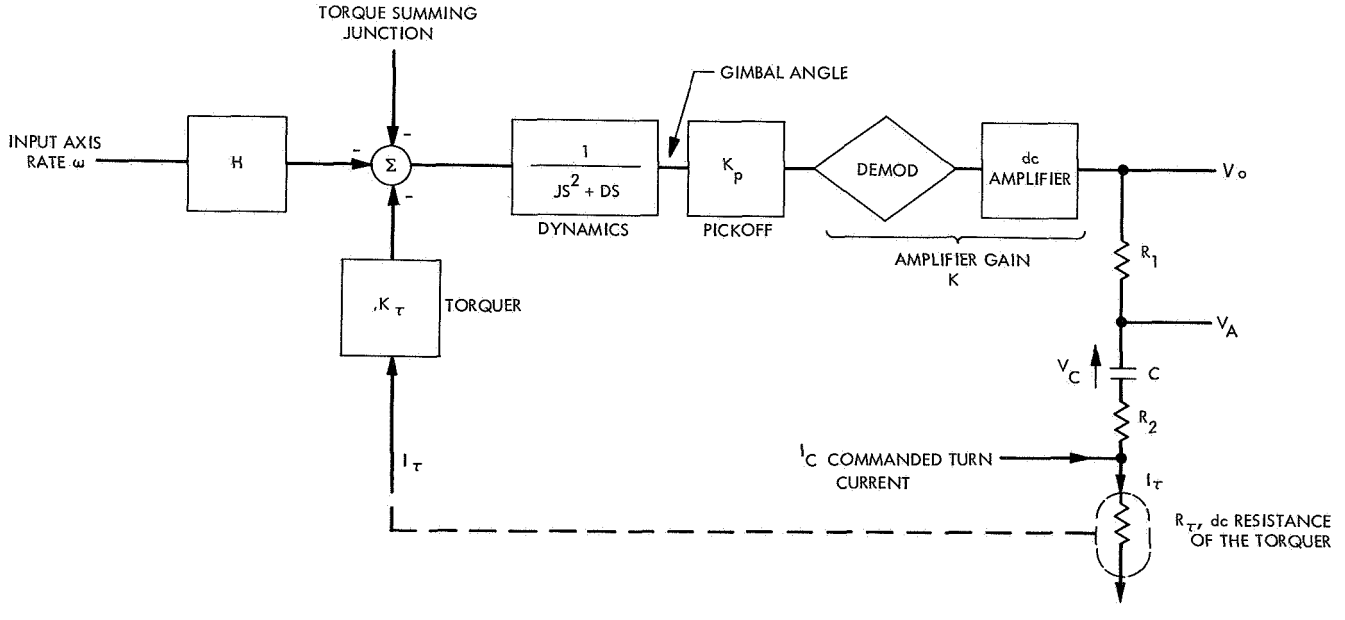

Fig. 15. *Mariner* gyro block diagram, position mode

The essentials of system operation can be seen by considering the rotation of the gyro about its input axis with $I_C = 0$. This produces an output-axis gimbal motion which is sensed by the pickoff. This signal is amplified and used to drive the torquer through an RC-series network, and the resulting current through the torquer captures the gimbal. For low-frequency inputs, the torquer current represents the input-angular rate divided by K_T/H. This current is integrated by the capacitor whose voltage becomes proportional to the input-axis angular excursions. The autopilot driving voltage V_a is thus made up of a position component V_C and a rate component $I_T (R_T + R_2)$. A position-plus-rate signal is always needed for autopilot stability.

The alternate system is to use a low-gain, "wide-angle" gyro in an open loop manner. The output will then be a pure position signal, and the needed rate component can be generated by using a lead or lead-lag circuit. This system was used by *Lunar Orbiter* where the wide-angle gyro was followed by an operational amplifier lead network with an α of 40.

The wide-angle gyro requires active temperature control by heating which is in contrast to the high-gain systems where the damping may vary from 500 to 2000 dyne cm s, producing only a ¼% change in position scale factor. Thus, the major tradeoff is between heaters and capacitors. The high-gain system has an advantage, however, which makes it desirable for the orbiter mission. This advantage is that high-rate-to-position mixing is easily obtained without increasing the gyro noise output; for *Mariner* spacecraft, a large-rate component is necessary to slow the system response enough to avoid exciting mechanical resonances.

I. Gyro loop equations. The dynamic equations for the high-gain gyro system can be determined by referring to Fig. 15. Here

$$I_T = \frac{V_o CS}{RCS + 1} + \left(\frac{R'CS + 1}{RCS + 1}\right) I_C$$

where

$$R \triangleq R_1 + R_2 + R_T$$

$$R' \triangleq R_1 + R_2$$

since

$$V_o = -\frac{(H\omega + K_T I_T) K K_p}{JS^2 + DS}$$

where

H = angular momentum

K_T = torquer scale factor

K = amplifier gain

K_p = pickoff scale factor

J = gimbal inertia

D = gimbal damping

Substitution yields

$$V_o = \frac{-(H K K_p)(RCS + 1)\frac{\omega}{S}}{JRCS^2 + (DRC + J)S + (K K_p K_T C + D)} - \frac{K K_p K_T (R'CS + 1)\frac{I_C}{S}}{JRCS^2 + (DRC + J)S + (K K_p K_T C + D)}$$

If the approximation is made that

$$\frac{H K K_p}{K K_p K_T C + D} \approx \frac{H}{K_T C}$$

then

$$V_o = \frac{-\left(\frac{H}{K_T C}\right)(RCS + 1)\frac{\omega}{S}}{\frac{JR}{K K_p K_T}S^2 + \frac{(DRC + J)}{K K_p K_T C}S + 1} - \frac{(R'CS + 1)\frac{I_C}{CS}}{\frac{JR}{K K_p K_T}S^2 + \frac{(DRC+J)}{K K_p K_T C}S + 1}$$

Since I_C is always zero for autopilot purposes, the voltage used as input to the autopilot is

$$V_A = \frac{-\left(\frac{H}{K_T C}\right)(R_A CS + 1)\frac{\omega}{S}}{\frac{JR}{K K_p K_T} S^2 + \frac{(DRC + J)}{K K_p K_T C} S + 1}$$

where

$$R_A = R_2 + R_T$$

Table 6 gives the parameters expected for the *Mariner* orbiter gyros.

2. Evaluation of the gyro model. If an average value of viscous damping, say 1020 dyn cm s, is selected, the natural frequency and damping factor of the gyro loop will appear to be

$$\omega_n = 58 \text{ rad/s}$$

$$\zeta = 0.043$$

Fortunately, these values do not predict the actual performance of the gyro. The block diagram in Fig. 15 is the conventional simplification of the actual gyro and most of the effects neglected are of the second order.

Table 6. *Mariner* orbiter gyro/GCA parameters

Parameter	Symbol	Value
Angular momentum	H	227,000 dyn cm s
Gain	H/D	235 ±25% ±3%/°F at 115°F
Torquer scale factor	K_T	303,148 dyn cm/A
Pickoff scale factor	K_p	159 mV/deg
Gimbal inertia	J	200 dyn cm s^2
Amplifier gain	K	200–500 V/V_{RMS}
Total torquer-series resistance	R	500 ohms
Padded torquer resistance	$R_T + R_2$	400 ohms
Torquer resistance	R_T	266 ohms
Natural frequency[a]	ω_g	88 rad/s
Damping[a]	ζ	0.35
Position scale factor	$H/K_T C$	2.9 V/deg at 115°F
Capacitance	C	0.00408 F nominal (0.00444 F typical)
Equivalent torquer scale factor	K_T	280°/h/mA

[a]Linear approximation at 115°F positioned IAE/OAH.

This model breaks down for high-gain gyros because one of these effects becomes first order. It can be seen that **H**, the angular momentum, does not appear in the gimbal-control loop, but appears only as an input gain. This would indicate that the response of the gimbal loop itself would be the same with the spin motor *on* or *off*. Indeed, if the spin motor is *off*, the response of the gimbal is very underdamped and approximately as predicted. However, when the wheel is spinning the situation is not as expected. This is because the motion of the gimbal is independent of **H** only if there is no motion of the wheel about the input axis when the gimbal is rotated. Since there must be clearance in the bearings (even though only microinches), the wheel does rotate about the input axis and an additional torque is experienced, at the gimbal, until the wheel is finally restrained. This pivot and jewel clearance effect is repeatable and does not differ much among gyros of the same type. The overall result is to make the gyro response nonlinear and to substantially raise the effective gimbal loop damping.

A typical *Mariner* gyro response and a linear approximation to it are shown in Fig. 16. The method of gyro analytical approximation which is usually employed is to

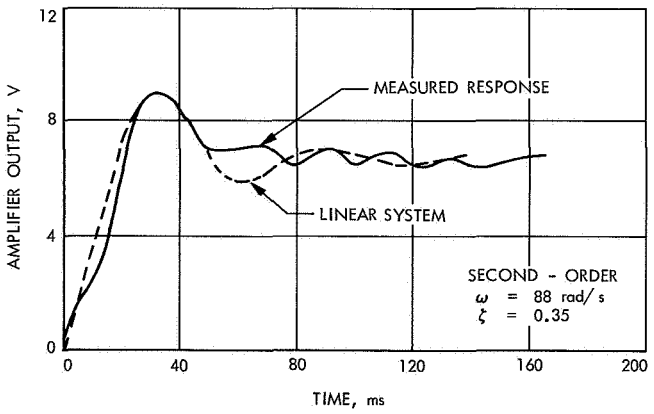

Fig. 16. Gyro step response

use the equations predicted by the linear model with the quadratic denominator replaced by a second-order system selected to more closely represent the actual gyro. For a typical gyro

$$\omega_n = 88 \text{ rad/s}$$
$$\zeta = 0.35$$

and for a conservative model

$$\omega_n = 51.5 \text{ rad/s}$$
$$\zeta = 0.241$$

3. Gyro model for system simulation and analysis. For systems work, the equations for commanded turns are modified to

$$V_o = \frac{-\omega_g^2 \left(\frac{H}{K_T C}\right)(RCS + 1)\frac{\omega}{S}}{S^2 + 2\zeta\,\omega_g S + \omega_g^2} - \frac{\omega_g^2 (R'CS + 1)\frac{I_c}{CS}}{S^2 + 2\zeta\,\omega_g S + \omega_g^2}$$

and the signal to the autopilot is given by

$$V_A = \frac{-\omega_g^2 \left(\frac{H}{K_T C}\right)(R_A CS + 1)\frac{\omega}{S}}{S^2 + 2\zeta\,\omega_g S + \omega_g^2}$$

(a) COMMANDED TURNS

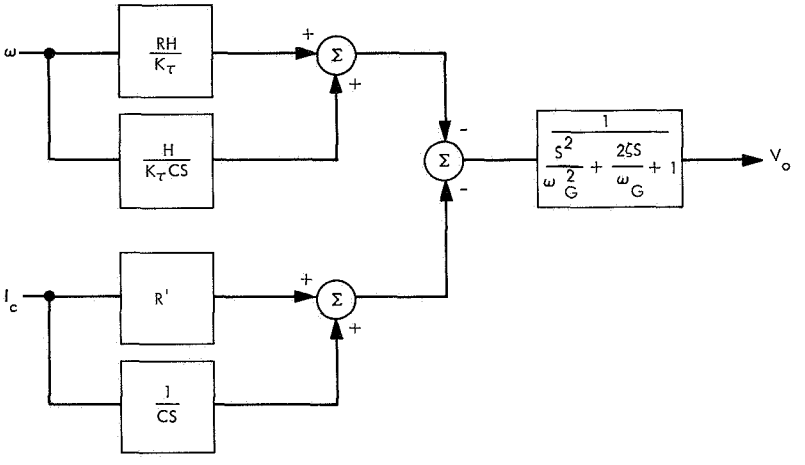

(b) AUTOPILOT OUTPUT

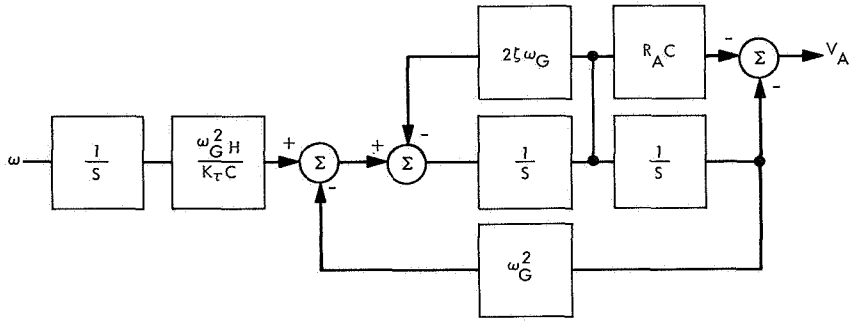

Fig. 17. Simulation block diagrams

These equations in block-diagram form, ready for computer simulation, are displayed in Fig. 17.

4. Gyro position scale factor. One of the more important parameters of the gyro loop is the position scale factor. This is the term

$$K_g = \frac{H}{K_T C}$$

For a *Mariner* orbiter this will be approximately 2.9 V/deg. Based upon past *Mariner* gyro history, it is expected that the actual gyros will have a standard deviation from this value of 0.18 V/deg.

The variation in scale factor during inflight operation is also important. The prime contributor to this variation is the change in capacitor value with temperature. Typical capacitor thermal characteristics are shown in Fig. 18. The overall effect, based upon measured data, is to produce a change in K_g of $-0.083\%/°F$. Thus, a $\pm 30°F$ range from the nominal temperature of 115°F produces a $\mp 2.5\%$ change in K_g. Past *Mariner* gyro-position scale factors and variations are summarized in Table 7.

Table 7. *Mariner* gyro-position scale-factor summary

(a) *Mariner* gyro-position scale-factor measurement repeatability, 115°F (*Mariner* Mars 1969 prototype)

Place of measurement	Date	V/deg		
		Pitch	Yaw	Roll
JPL	4/11/68	5.31	5.95	5.96
Honeywell	—	5.3641	6.0175	6.012
Percent difference: 1.01, 1.12, 0.87.				
Average: 1.0%.				

(b) *Mariner* gyro-position scale factors, 115°F

GCA S/N	Spacecraft	Date	V/deg		
			Pitch	Yaw	Roll
015	*Mariner IV*	5/27/64	5.64	5.73	5.10
016	*Mariner* Venus 67	10/11/66	6.046	6.0654	6.2185
017	*Mariner* Venus 67	7/27/66	6.467	6.194	5.852
0001	*Mariner* Mars 1969, proto	4/11/68	5.31	5.95	5.96
Average: 5.878%.					
Standard deviation: 0.37.					

(c) *Mariner* gyro-position scale-factor variation with temperature (*Mariner* Mars 1969 prototype)

Temperature	Date	V/deg		
		Pitch	Yaw	Roll
85°F	4/12/68	5.4467	6.0989	6.1127
115°F	4/11/68	5.31	5.95	5.96
Average temperature coefficient: −0.0049 V/deg/°F.				

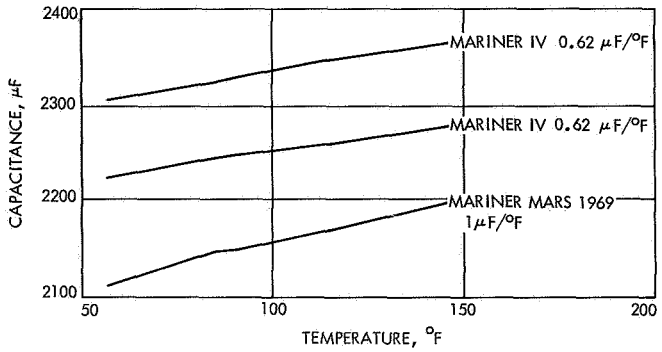

Fig. 18. *Mariner* gyro integrating capacitor thermal characteristics, 1/2 channel

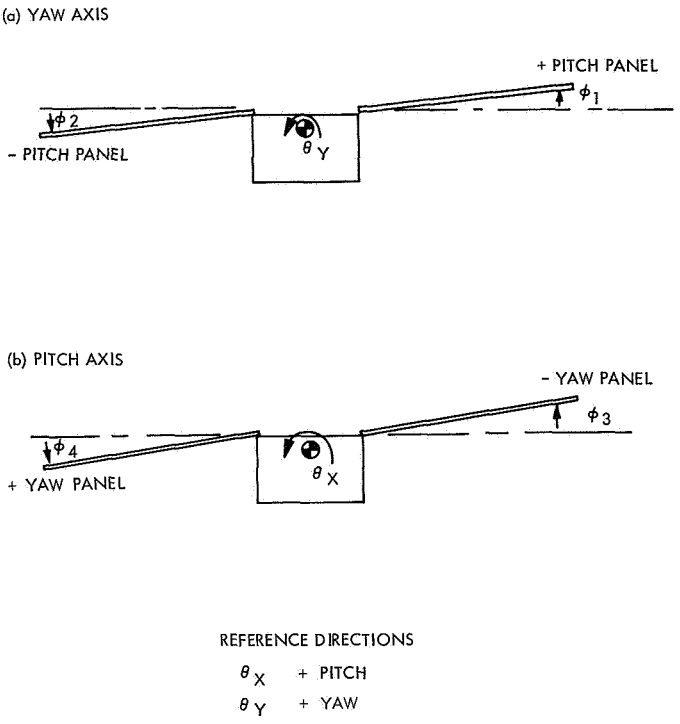

Fig. 19. Solar panel flexure angles

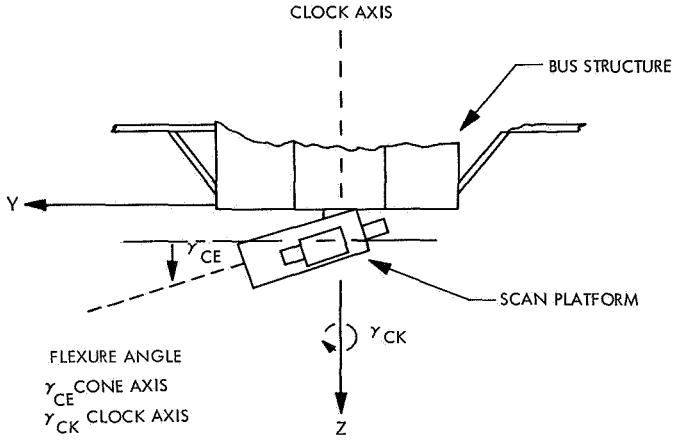

Fig. 20. Scan platform flexure angles

B. *Structural Dynamics*

There are five flexible members on the *Mariner* orbiter with natural frequencies low enough to be a potential problem to the autopilot system. These are the four solar panels and the scan platform. The solar panels are hinged to the spacecraft and when deployed they are controlled in hinge axis bending by the cruise dampers. The fundamental bending mode of the panel itself and its fundamental torsional mode are fortunately high enough in frequency so as not to be a problem. The only solar-panel mode of importance to the autopilot system is hinge bending. The characteristics of this mode are determined mainly by the hinge-axis panel moment of inertia and the damper parameters. A cruise damper is a spring-dashpot device which when attached to a panel controls, within limits, the natural frequency and damping of the hinged panel. The spring constant is linear, but the damping term contains both a linear, viscous term and a coulomb friction term. The *Mariner* orbiter panel configuration and the definitions of the panel flexure angles are shown in Fig. 19.

The other flexible member of importance, the scan platform, has two bending modes. These modes are about the two mutually perpendicular actuator-driven axes, clock and cone. The platform can flex about these axes due to compliance in the actuators and supporting structure. The scan platform is shown in its stowed position in Fig. 20. It is assumed that the platform will be driven to this position for each velocity correction maneuver. The angles γ_{CE} and γ_{CK} are the cone and clock deflections of the scan platform with the drive actuators de-energized.

1. Structural dynamics mathematical model. The definitions illustrated in Figs. 19 and 20 are combined into a structural dynamics model in Fig. 21. Important structural parameters are further defined in Table 8. It is now possible to write the equations governing this model. One of the assumptions under which these relations will be derived is that all the angles involved will be small and that the usual small-angle approximations will be valid. Another approximation is that the flexing of the structure will not significantly change the composite CG in the spacecraft-coordinate system.

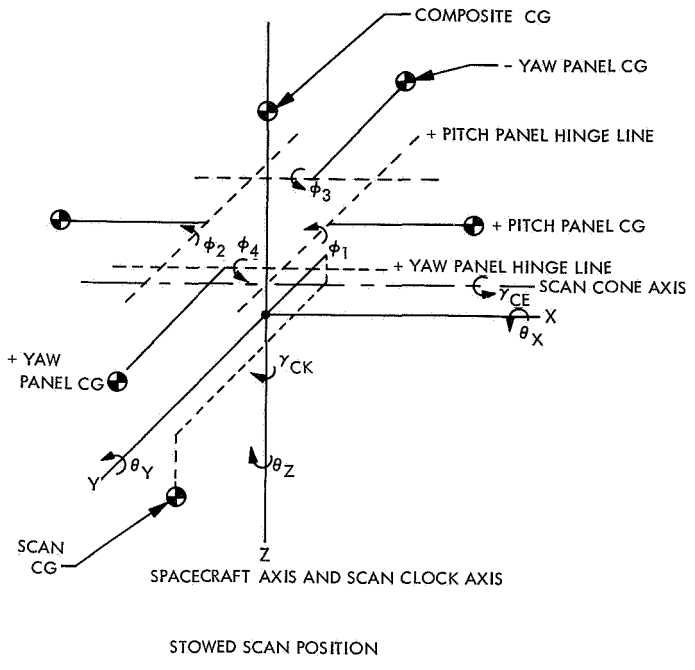

Fig. 21. Structural dynamics model

The torques on the flexible members produced by the translation of the spacecraft are given by

$$
\begin{aligned}
T_1 &= +M_p L_{p2} \ddot{Z} \\
T_2 &= -M_p L_{p2} \ddot{Z} \\
T_3 &= +M_p L_{p2} \ddot{Z} \\
T_4 &= -M_p L_{p2} \ddot{Z} \\
T_{CE} &= +M_S L_{S3} \ddot{Y} - M_S L_{S2} \ddot{Z} \\
T_{CK} &= +M_S L_{S1} \ddot{X}
\end{aligned}
$$

Along with these torques are the rotation induced torques

$$
\begin{aligned}
T'_1 &= -M_p \ddot{\theta}_y L_{p1} L_{p2} - I_p \ddot{\theta}_y \\
T'_2 &= -M_p \ddot{\theta}_y L_{p1} L_{p2} - I_p \ddot{\theta}_y \\
T'_3 &= -M_p \ddot{\theta}_x L_{p1} L_{p2} - I_p \ddot{\theta}_x \\
T'_4 &= -M_p \ddot{\theta}_x L_{p1} L_{p2} - I_p \ddot{\theta}_x \\
T'_{CE} &= -M_S \ddot{\theta}_x L_{S1} L_{S2} - M_S \ddot{\theta}_x L_{S3} L_{S4} - I_{CE} \ddot{\theta}_x \\
T'_{CK} &= +M_S \ddot{\theta}_y L_{S1} L_{S4} - I_{CKA} \ddot{\theta}_z
\end{aligned}
$$

The reaction torques produced about the spacecraft center of mass as a result of the structural deformation are

Table 8. Definitions for the structural dynamics model

Symbol	Definition
XS	Scan platform spacecraft X axis CG location
YS	Scan platform spacecraft Y axis CG location
ZS	Scan platform spacecraft Z axis CG location
YCE	Cone axis spacecraft Y axis component
ZCE	Cone axis spacecraft Z axis component
ZCG	Spacecraft Z axis location of the composite CG
L_{S1}	YS
L_{S2}	YS-YCE
L_{S3}	ZS-ZCE
L_{S4}	ZS-ZCG
L_{p1}	Distance spacecraft Z axis to panel CG
L_{p2}	Distance hinge line to panel CG
I_p	Panel moment of inertia
I_{CK}	Scan clock moment of inertia
I_{CE}	Scan cone moment of inertia
I_H	Panel moment of inertia about hinge
I_{CKA}	Scan moment of inertia about clock axis
I_{CEA}	Scan moment of inertia about cone axis
M_p	Mass of a solar panel
M_S	Mass of the scan platform
I_{XX}	Spacecraft composite pitch moment of inertia
I_{YY}	Spacecraft composite yaw moment of inertia
I_{ZZ}	Spacecraft composite roll moment of inertia

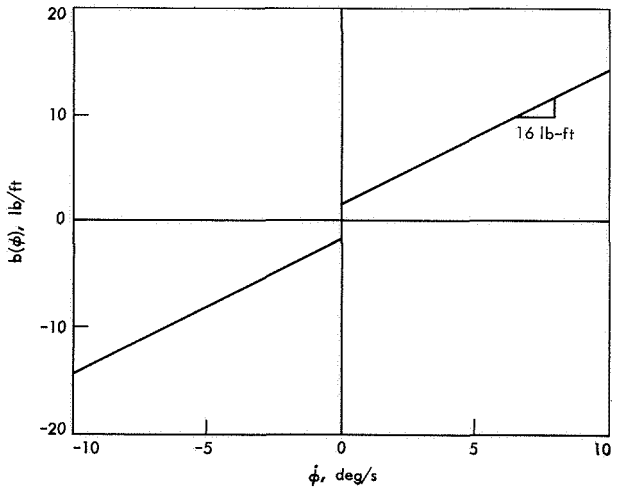

Fig. 22. Solar panel damping torque

$$
\begin{aligned}
T_X &= -(M_p L_{p1} L_{p2} + I_p)(\ddot{\phi}_3 + \ddot{\phi}_4) \\
&\quad -(M_S L_{S1} L_{S2} + M_S L_{S3} L_{S4} + I_{CE})\ddot{\gamma}_{CE} \\
T_Y &= -(M_p L_{p1} L_{p2} + I_p)(\ddot{\phi}_1 + \ddot{\phi}_2) \\
&\quad +M_S L_{S1} L_{S4} \ddot{\gamma}_{CK} \\
T_Z &= -I_{CKA} \ddot{\gamma}_{CK}
\end{aligned}
$$

The panels are restrained by the cruise dampers, which produce a spring-restoring torque and a nonlinear damping. A typical damping function $b(\dot{\phi})$ is shown in Fig. 22. The scan platform rotation is restrained by equivalent spring constants and small linear dampings. These restraining torques are

$$
\begin{aligned}
T_1'' &= -I_H \ddot{\phi}_1 - b_1(\dot{\phi}) - K_1 \phi_1 \\
T_2'' &= -I_H \ddot{\phi}_2 - b_2(\dot{\phi}_2) - K_2 \phi_2 \\
T_3'' &= -I_H \ddot{\phi}_3 - b_3(\dot{\phi}_3) - K_3 \phi_3 \\
T_4'' &= -I_H \ddot{\phi}_4 - b_4(\dot{\phi}_4) - K_4 \phi_4 \\
T_{CE}'' &= -I_{CEA} \ddot{\gamma}_{CE} - b_{CE} \gamma_{CE} - K_{CE} \gamma_{CE} \\
T_{CK}'' &= -I_{CKA} \ddot{\gamma}_{CE} - b_{CK} \gamma_{CK} - K_{CK} \gamma_{CK}
\end{aligned}
$$

consistent with the small angle assumptions

$$
\begin{aligned}
I_{XX} \ddot{\theta}_x &= N_x + T_x \\
I_{YY} \ddot{\theta}_y &= N_y + T_y \\
I_{ZZ} \ddot{\theta}_z &= N_z + T_z
\end{aligned}
$$

where N_x, N_y, N_z are the torques applied to the bus structure. If the following definitions are made

$$
\begin{aligned}
C_1 &= M_p L_{p2} \\
C_2 &= M_S L_{S3} \\
C_3 &= M_S L_{S2} \\
C_4 &= M_S L_{S1} \\
I_{p1} &= M_p L_{p1} L_{p2} + I_p \\
I_{S1} &= M_S L_{S1} L_{S2} + M_S L_{S3} L_{S4} + I_{CE} \\
I_{S2} &= M_S L_{S1} L_{S4}
\end{aligned}
$$

then the system equations become

$$
+C_1 \ddot{Z} - I_{p1} \ddot{\theta}_Y - I_H \ddot{\phi}_1 - b_1(\dot{\phi}_1) - K_1 \phi_1 = 0 \qquad (1)
$$

$$
-C_1 \ddot{Z} - I_{p1} \ddot{\theta}_Y - I_H \ddot{\phi}_2 - b_2(\dot{\phi}_2) - K_2 \phi_2 = 0 \qquad (2)
$$

$$
+C_1 \ddot{Z} - I_{p1} \ddot{\theta}_X - I_H \ddot{\phi}_3 - b_3(\dot{\phi}_3) - K_3 \phi_3 = 0 \qquad (3)
$$

$$
-C_1 \ddot{Z} - I_{p1} \ddot{\theta}_X - I_H \ddot{\phi}_4 - b_4(\dot{\phi}_4) - K_4 \phi_4 = 0 \qquad (4)
$$

$$
C_2 \ddot{Y} - C_3 \ddot{Z} - I_{S1} \ddot{\theta}_X - I_{CEA} \ddot{\gamma}_{CE} - b_{CE} \dot{\gamma}_{CE} - K_{CE} \gamma_{CE} = 0 \qquad (5)
$$

$$
C_4 \ddot{X} + I_{S2} \ddot{\theta}_Y - I_{CKA} \ddot{\theta}_Z - I_{CKA} \ddot{\gamma}_{CK} - b_{CK} \dot{\gamma}_{CK} - K_{CK} \gamma_{CK} = 0 \qquad (6)
$$

$$
I_{XX} \ddot{\theta}_X = N_X - I_{p1}(\ddot{\phi}_3 + \ddot{\phi}_4) - I_{S1} \ddot{\gamma}_{CE} \qquad (7)
$$

$$
I_{YY} \ddot{\theta}_Y = N_Y - I_{p1}(\ddot{\phi}_1 + \ddot{\phi}_2) + I_{S2} \ddot{\gamma}_{CK} \qquad (8)
$$

$$
I_{ZZ} \ddot{\theta}_Z = N_Z - I_{CKA} \ddot{\gamma}_{CK} \qquad (9)
$$

2. ***Structural dynamics in simulation form.*** To perform a proper digital simulation, values must be computed before they are needed; otherwise a one-step computational delay is introduced. Aside from the error thus produced, this type of delay tends to upset the error tolerance checks in adaptive numerical integrators and cause the selection of much smaller step sizes than are actually necessary. Therefore, it is imperative that the equations in the preceding section be sequenced for proper simulation. With some algebraic manipulation these equations can be simultaneously solved for the body axis rotations:

$$
\begin{aligned}
\ddot{\theta}_x = \frac{1}{I_{S3}} \Bigg\{ & N_X + \frac{I_{p1}}{I_H} [b_3(\dot{\phi}_3) \\
& + b_4(\dot{\phi}_4) + K_3 \phi_3 + K_4 \phi_4] \\
& + \frac{I_{S1}}{I_{CEA}} (C_3 \ddot{Z} - C_2 \ddot{Y} \\
& + b_{CE} \dot{\gamma}_{CE} + K_{CE} \gamma_{CE}) \Bigg\}
\end{aligned}
$$

Since $\ddot{X}$, $\ddot{Y}$, and $\ddot{Z}$ are already known by $\ddot{X} = F_X/M$, etc., $\ddot{\theta}_X$ can be solved for and the result integrated twice to produce rate and position. The term I_{S3} is defined as

$$
I_{S3} = I_{XX} - \frac{2I_{p1}^2}{I_H} - \frac{I_{S1}^2}{I_{CEA}}
$$

Proceeding in the same manner, the terms can be defined as

$$I_{S4} = I_{YY} - \frac{2I_{p1}}{I_H} - \frac{I_{S2}^2}{I_{CKA}}$$

$$I_{S5} = I_{ZZ} - I_{CKA}$$

$$U_1 = N_y + \frac{I_{p1}}{I_H}\left[b_1(\dot{\phi}_1) + b_2(\dot{\phi}_2) + K_1\phi_1 + K_2\phi_2\right] + \frac{I_{S2}}{I_{CKA}}\left(C_4\ddot{X} - b_{CK}\dot{\gamma}_{CK} - K_{CK}\gamma_{CK}\right)$$

$$U_2 = N_Z - C_4\ddot{X} + b_{CK}\dot{\gamma}_{CK} + K_{CK}\gamma_{CK}$$

The results are

$$\ddot{\theta}_Y = \frac{I_{S5}U_1 - I_{S2}U_2}{I_{S4}I_{S5} - I_{S2}^2}$$

$$\ddot{\theta}_Z = \frac{I_{S4}U_2 - I_{S5}U_1}{I_{S4}I_{S5} - I_{S2}^2}$$

With these terms solved, they may be used to determine the flexure angles and rates by direct substitution, as follows:

$$\ddot{\theta}_1 = \frac{\left[+C_1\ddot{Z} - I_{p1}\ddot{\theta}_y - b_1(\dot{\phi}_1) - K_1\phi_1\right]}{I_H}$$

$$\ddot{\theta}_2 = \frac{\left[-C_1\ddot{Z} - I_{p1}\ddot{\theta}_y - b_2(\dot{\phi}_2) - K_2\phi_2\right]}{I_H}$$

$$\ddot{\theta}_3 = \frac{\left[+C_1\ddot{Z} - I_{p1}\ddot{\theta}_x - b_3(\dot{\phi}_3) - K_3\phi_3\right]}{I_H}$$

$$\ddot{\theta}_4 = \frac{\left[-C_1\ddot{Z} - I_{p1}\ddot{\theta}_x - b_4(\dot{\phi}_4) - K_4\phi_4\right]}{I_H}$$

$$\ddot{\gamma}_{CE} = \frac{\left(C_2\ddot{Y} - C_3\ddot{Z} - I_{S1}\ddot{\theta}_x - b_{CE}\gamma_{CE} - K_{CE}\gamma_{CE}\right)}{I_{CEA}}$$

$$\ddot{\gamma}_{CK} = \frac{\left(C_4\ddot{X} + I_{S2}\ddot{\theta}_y - I_{CKA}\ddot{\theta}_Z - b_{CK}\dot{\gamma}_{CK} - K_{CK}\gamma_{CK}\right)}{I_{CKA}}$$

The foregoing method of solution is certainly not neat or elegant, but it is efficient.

3. Structural dynamics in decoupled linear form. In order to estimate the performance of the autopilot it is necessary to find a linear approximation to the structural dynamics which is devoid of coupling between axes. The rationale behind this is that the autopilot loops should be set up using the simplest model possible and then checked by simulation. This made it possible to linearize the panel damping, eliminate translational–rotational coupling, and concentrate on the pitch axis where the scan platform dynamics do not couple to the roll axis. A further simplification is made in that the solar panels are considered separately from the scan platform. The simplified Eq. (7) is transformed by Laplace's method as

$$I_{XX}\theta_X = \frac{N_X}{S^2} - I_{p1}(\phi_2 + \phi_4)$$

From Eqs. (3) and (4)

$$\phi_3 = \left(\frac{-I_{p1}S^2}{I_H S^2 + b_3 S + K_3}\right)\theta_X$$

$$\phi_4 = \left(\frac{-I_{p1}S^2}{I_H S^2 + b_4 S + K_4}\right)\theta_X$$

Substituting

$$\theta_X = \frac{N_X}{I_{XX}S^2}\left[\frac{\left(\frac{I_H}{K_3}S^2 + \frac{b_3}{K_3}S + 1\right)\left(\frac{I_H}{K_4}S^2 + \frac{b_4}{K_4}S + 1\right)}{P_4S^4 + P_3S^3 + P_2S^2 + P_1S + 1}\right]$$

where

$$P_4 = \frac{I_H^2 I_{XX} - 2I_{p1}^2 I_H}{I_{XX}K_3K_4}$$

$$P_3 = \frac{(I_H I_{XX} - I_{p1}^2)(b_3 + b_4)}{I_{XX} K_3 K_4}$$

$$P_2 = \frac{(I_H I_{XX} - I_{p1}^2)(K_3 + K_4) + I_{XX} b_3 b_4}{I_{XX} K_3 K_4}$$

$$P_1 = \frac{b_3 K_4 + b_4 K_3}{K_3 K_4}$$

Returning to Eq. (7) for the scan platform dynamics

$$I_{XX}\,\theta_X = \frac{N_X}{S^2} - I_{S1}\,\gamma_{CE}$$

and from Eq. (5)

$$\gamma_{CE} = \left(\frac{-I_{S1} S^2}{I_{CEA} S^2 + b_{CE} S + K_{CE}}\right)\theta_X$$

combining

$$\theta_X = \frac{N_X}{I_{XX} S^2}\left[\frac{\frac{I_{CEA}}{K_{CE}} S^2 + \frac{b_{CE}}{K_{CE}} S + 1}{\left(\frac{I_{CEA} I_{XX} - I_{S1}^2}{I_{XX} K_{CE}}\right) S^2 + \frac{b_{CE}}{K_{CE}} S + 1}\right]$$

Now with the assumed decoupling between the scan platform and the solar panels, the scan platform and solar panels can be considered series elements with

$$N'_X = \left[\frac{\left(\frac{I_H}{K_3} S^2 + \frac{b_3}{K_3} S + 1\right)\left(\frac{I_H}{K_4} S^2 + \frac{b_4}{K_4} S + 1\right)}{P_4 S^4 + P_3 S^3 + P_2 S^2 + P_1 S + 1}\right] N_X$$

$$N''_X = \left[\frac{\frac{I_{CEA}}{K_{CE}} S^2 + \frac{b_{CE}}{K_{CE}} S + 1}{\left(\frac{I_{CEA} I_{XX} - I_{S1}}{I_{XX} K_{CE}}\right) S^2 + \frac{b_{CE}}{K_{CE}} S + 1}\right] N'_X$$

and

$$\theta_X = \frac{N''_X}{I_{XX} S^2}$$

The justification for doing this follows. If Eqs. (3), (4), (5), and (7) were solved simultaneously, a sixth-order denominator would result instead of separate fourth- and second-order denominators. The factored, sixth-order polynomial, however, would have approximately the same poles as obtained by factoring and multiplying the second- and fourth-order polynomials separately. The pitch-axis structural block diagram is shown in Fig. 23.

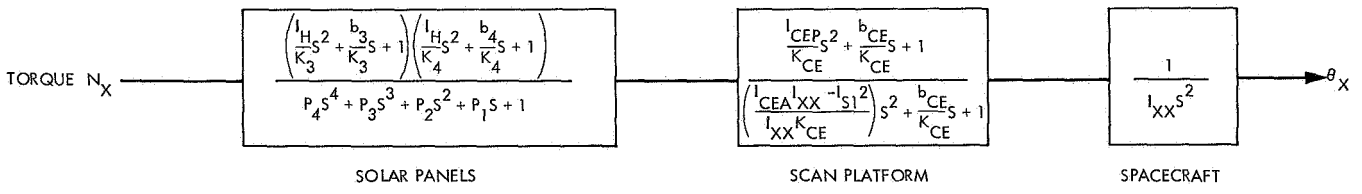

PITCH AXIS

$$P_4 = \frac{I_{XX} I_H^2 - 2 I_H I_{P1}^2}{I_{XX} K_3 K_4}$$

$$P_3 = \frac{\left(I_H I_{XX} - I_{P1}^2\right)(b_3 + b_4)}{I_{XX} K_3 K_4}$$

$$P_2 = \frac{\left(I_H I_{XX} - I_{P1}^2\right)(K_3 + K_4) + I_{XX} b_3 b_4}{I_{XX} K_3 K_4}$$

$$P_1 = \frac{b_3 K_4 + b_4 K_3}{K_3 K_4}$$

Fig. 23. Simplified spacecraft structural dynamics block diagram

4. Other spacecraft dynamics. There are two other dynamic effects due to spacecraft structure which are not included in this model; these are:

(1) The "tail wags dog" effect.

(2) Fuel slosh.

The first effect refers to the disturbance felt by the spacecraft when the engine is moved by the gimbal actuators. This effect is negligible primarily because the engine is small relative to the spacecraft. The gimballed mass of the engine is only about 30 lb with a moment of inertia of less than 0.1 slug ft^2. The equations governing this effect and their application are treated in Appendix F.

The fuel slosh effect also appears to be negligible at this time. It will be important, however, to verify this conclusion when better data for the fuel slosh model becomes available.

C. Generalized Model for the Gimbal Servo

It is necessary to produce models of the gimbal servo for simulation and analysis which are general enough to provide accurate modeling without being dependent upon particular mechanizations. There are essentially three characteristics which must be included for a gimbal servo model which exhibits the major characteristics of actual hardware:

(1) The linear dynamic response of the motor/lead-screw system.

(2) The saturation of the drive amplifier which limits the maximum slew rate.

(3) The motor threshold voltage necessary to start the gimbal moving.

1. Simulation model. A general block diagram of a gimbal servo is presented in Fig. 24. The gain K_{DV} represents the input resistor to the drive amplifier K_A which saturates at E_{SAT}. The amplifier output is fed to the armature of the motor which is modeled by a double integration with nonlinear-rate feedback. This feedback has a coulomb friction level E_T and a linear term S_G. The linear term represents the back EMF of the motor and the linear component of friction. The gimbal position is sensed by a transducer and fed back through a gain K_{PF} plus a lead term T_{FG}. This represents a lead compensator consisting of a parallel resistor-capacitor input to the drive amplifier. It is interesting to note that this overall model would still hold if the drive to the motor were pulse-width modulated.

The parameters for this model can be easily calculated from the performance parameters of the actuator and the gains of the drive amplifier. The threshold voltage necessary to start the gimbal moving is E_T, and this varies with the actuator force required. Unfortunately, an estimated average value of E_T has to be used because the major load on the actuator is the propellant-line bending force which is difficult to predict until an actual test configuration is constructed. The S_G can be determined from

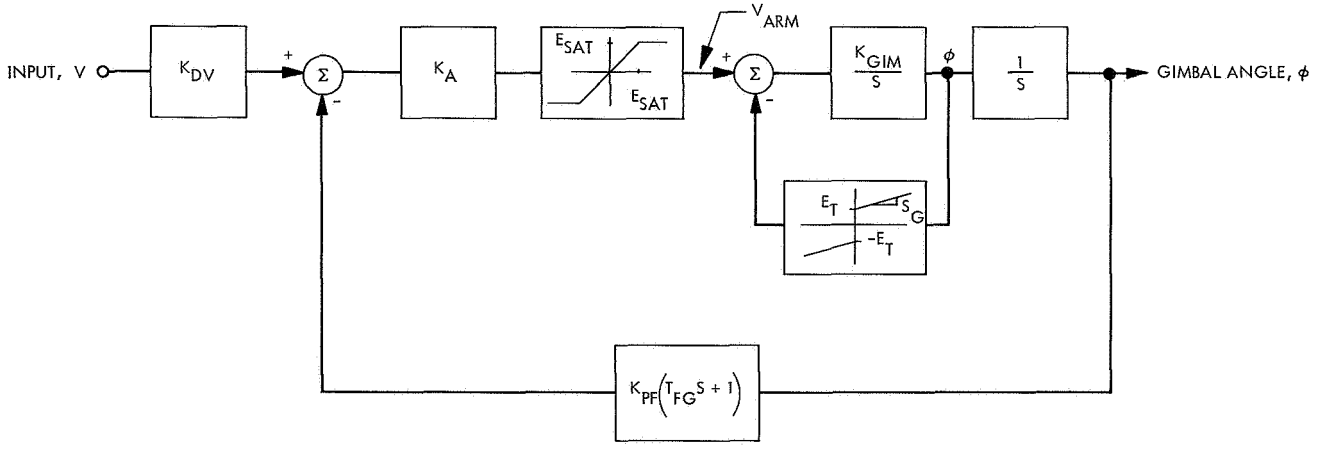

Fig. 24. General gimbal servo model

the maximum slew rate of the gimbal when E_{SAT} is applied to the motor. Thus,

$$S_G = \frac{E_{SAT} - E_T}{\omega_m}$$

where ω_m is the maximum slew rate. The motor constant K_{GIM} is made up of armature resistance, torque constant, and load inertia. Experimentally, it can be determined from the time constant of the motor in reaching ω_m. If T_m is this time constant, then

$$K_{GIM} = \frac{1}{T_m S_G}$$

T_{FG}, K_{PF}, K_A, and K_{DV} are set by the amplifier resistor and capacitor selection. The dc gain of the servo is

$$K_{GS} = \frac{K_{DV}}{K_{PF}} \text{ rad/V}$$

and along with this is the electrical resolution

$$\phi_E = \frac{E_T}{K_{PF}K_A} \text{ rad}$$

which corresponds to

$$V_E = \frac{E_T}{K_{DV}K_A} \text{ V (referred to the input)}$$

The mechanical backlash is not included in this resolution.

The model for nonlinear-rate feedback shown in Fig. 24 is the conventional representation given in textbooks. It is, however, an extremely poor way of representing the characteristics of a motor on a digital computer. The jump discontinuity at zero in the rate feedback can cause oscillations at the period of the integration step size. With an adaptive predictor/corrector numerical-integration routine, this causes an intolerable reduction in step size. One method sometimes employed to stop this oscillation is to change the discontinuity into a finite slope. This unfortunately provides little relief from step-size shrinkage because the large slope implies a short time constant; this is also unsuitable for numerical integration. One way to approach this problem is to consider what this characteristic represents in the actual hardware. What this is modeling is the fact that when the gimbal rate is very low and the armature voltage is less than the threshold, the gimbal seizes due to friction.

In the actual servo, the motion does stop suddenly, and this is accurately modeled in Fig. 24 where it is almost instantaneous. Realizing that the speed of seizure of the gimbal is not very important to the overall system model, one could use the natural time constant of the motor T_m to effect this and still have a reasonably accurate dynamic representation. When the gimbal servo is in operation the adaptive integration routine must have a step size suitable for integrating dynamics with a time constant of T_m, and, thus, when the gimbal motion is stopped by a friction characteristic containing the same time constant, the step size will not be compromised.

A motor model suitable for simulation is shown in Fig. 25. In this model the voltage value of coulomb friction is subtracted from the input voltage and this signal ε is fed to a multiplier. The other multiplier input comes from an inclusive OR gate so the output of the multiplier is either zero or ε. This signal is then fed to a linear model of the motor. Thus, if the armature voltage is less than the threshold and the rate is less than an arbitrary low rate ω_T, the gimbal seizes with a time constant of T_M.

2. *Linear servo model for analysis.* A linear analytical model of the gimbal servo is needed for preliminary system design. If the input signal to the system is of the magnitude to produce an armature voltage mainly between E_T and E_{SAT} and does not saturate the amplifier for significant periods, then the nonlinearities can be neglected and an approximate transfer function is determined. It will be important, however, to test the validity of any model so derived before relying upon the results. As is often done, this approximation can be carried further, but the foregoing has done enough injustice to linear theory. This is certainly true in light of modern simulation techniques. A linear approximation is then

$$H(S) = \frac{\frac{K_{DV}}{K_{PF}}}{\left(\frac{1}{K_{GIM}\,K_A\,K_{PF}}\right)S^2 + \left(\frac{S_G + K_A\,K_{PF}\,T_{FG}}{K_A\,K_{PF}}\right)S + 1}$$

3. *Low-frequency describing-function model.* It is expected that the autopilot system will exhibit limit-cycle operation because of the thresholds in the gimbal actuators. To aid in the determination of the period and amplitude of this oscillation, a low-frequency describing function will be determined between V_{ARM} and ε for the system in Fig. 25. Let V_{ARM} be a sinusoidal signal

$$V_{ARM} = A \sin \omega t$$

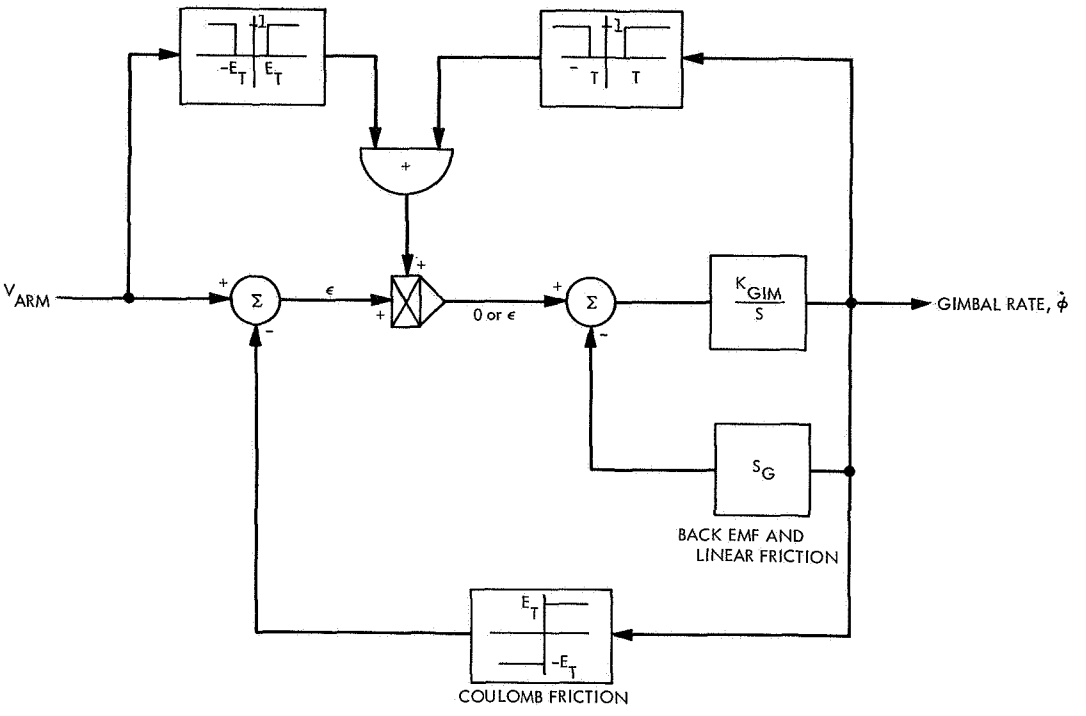

Fig. 25. Computer model for actuator drive

where

$$A < E_{SAT}$$

and

$$\omega << \frac{1}{K_{GIM}\, S_G}$$

Under these conditions there will be negligible phase shift and the signal ε will be given by

$$\varepsilon = 0;\ V_{ARM} < E_T$$

$$\varepsilon = A \sin \omega t - E_T;\ V_{ARM} > E_T$$

If $A > E_T$, then ε is an odd function with 1/2-λ symmetry. The fundamental component magnitude is

$$b_1 = \frac{4}{\pi} \int_0^{\pi/2} \varepsilon(t) \sin \omega t\, d(\omega t)$$

If α is defined

$$\alpha \triangleq \sin^{-1}\left(\frac{E_T}{A}\right)$$

then,

$$b_1 = \frac{4}{\pi} \int_\alpha^{\pi/2} (A \sin \omega t - E_T) \sin \omega t\, d(\omega t)$$

and

$$b_1 = 0;\ A < E_T$$

$$b_1 = A\left(1 - \frac{2\alpha}{\pi} + \frac{\sin 2\alpha}{\pi} - \frac{E_T}{A} \cos \alpha\right);\ A > E_T$$

This describing function is plotted in Fig. 26 as a function of normalized input.

4. Gimbal servo model verification. The performance characteristics of the *Lunar Orbiter* gimbal servo were used to verify the analytical models. This ±3-deg Kearfott[1] servo is shown in Fig. 27 along with its performance parameters. The model parameters are computed from these values.

$$K_{DV} = 1/18 = 0.05555 \text{ mA/V}$$

$$K_{PF} = (1/94.5)\ (52.5)\ (5.6) = 3.111 \text{ mA/rad}$$

$$T_{FG} = (0.6)\ (0.0945) = 0.056 \text{ s}$$

$$K_A = (16)\ (180) = 2880 \text{ V/mA}$$

[1]Kearfott Division, General Precision, Inc.

E_{SAT} = 28 V

E_T = 7 V

ω_m = (1.11) (1/5.6) = 0.198 rad/s

S_G = 106 V/rad/s

K_{GIM} = 0.27 rad/s²/V

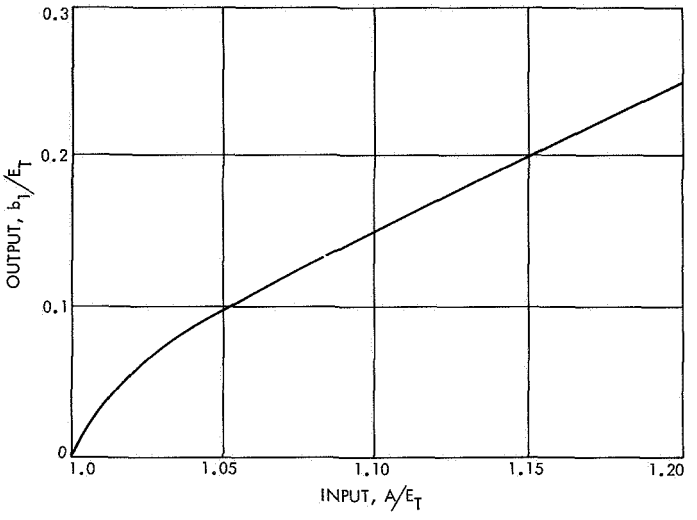

Fig. 26. Actuator describing function

These yield a linearized model of

$$H(S) = \frac{0.01786}{0.00059S^2 + 0.0678S + 1}$$

Here, the natural frequency is 6.5 Hz with a damping factor of 1.39. The nonlinear analytical model was simulated on the IBM 7094 using the DSL/90 language. A 4.0-V step was applied to the model and the result is shown in Fig. 28. The data points plotted represent actual test data reported by Kearfott. From this it can be seen that the simulated model is reasonably accurate. A comparison was then made between the nonlinear and linear models for a small gimbal angle step of 0.3 deg. It can be seen that for small excursions the linear model is satisfactory; this is shown in Fig. 29. The same comparison for a 2-deg step is presented in Fig. 30.

D. Force and Torque Equations

1. Complete force and torque equations. To determine the torque imparted to the spacecraft by the engine, the gimbal angles will be defined as shown in Fig. 31; ϕ_x is the pitch-gimbal angle, ϕ_y is the yaw-gimbal angle, and

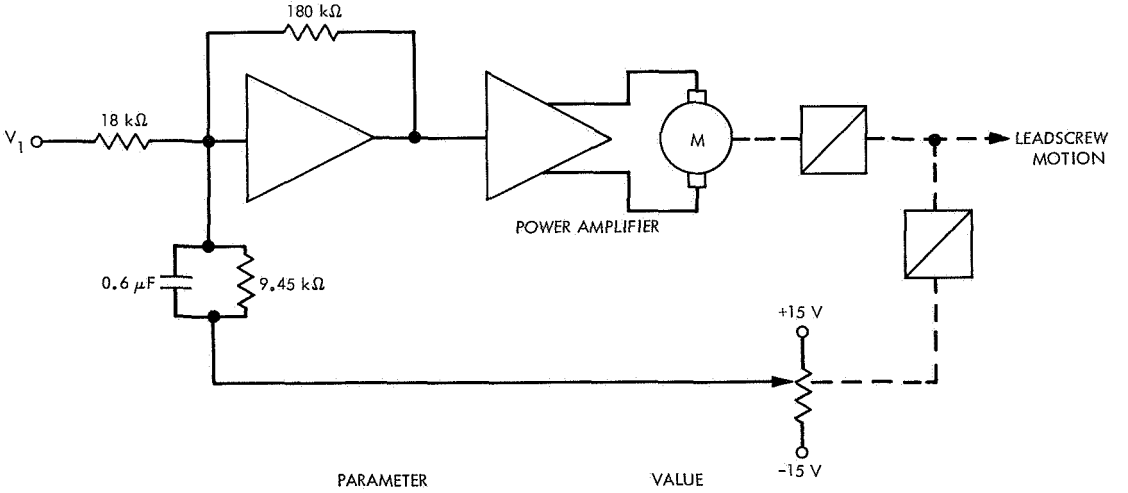

PARAMETER	VALUE
POWER AMPLIFIER GAIN	16 V/V
MOTOR THRESHOLD, E_T	7.0 V
LINEAR TRAVEL OF LEADSCREW	±0.293 in.
LINEAR RATE AT 28 V	1.11 in./s
LEVER ARM OF ACTUATOR	5.6 in.
POTENTIOMETER SCALE FACTOR	52.5 V/in.
MOTOR TIME CONSTANT	0.035 s

Fig. 27. Kearfott gimbal servo used on *Lunar Orbiter*

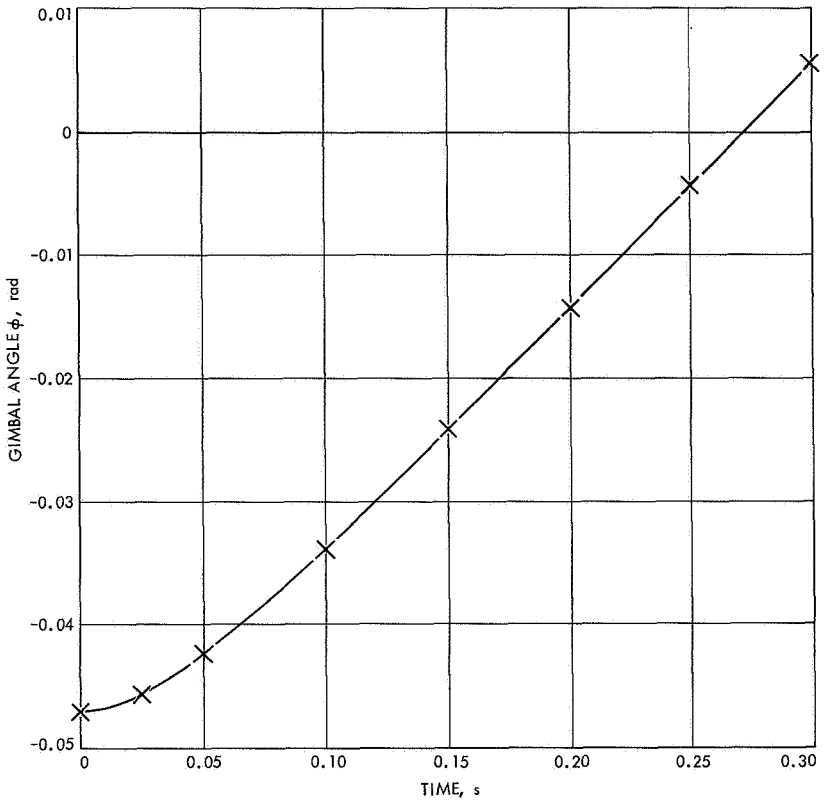

Fig. 28. Gimbal position with measured data

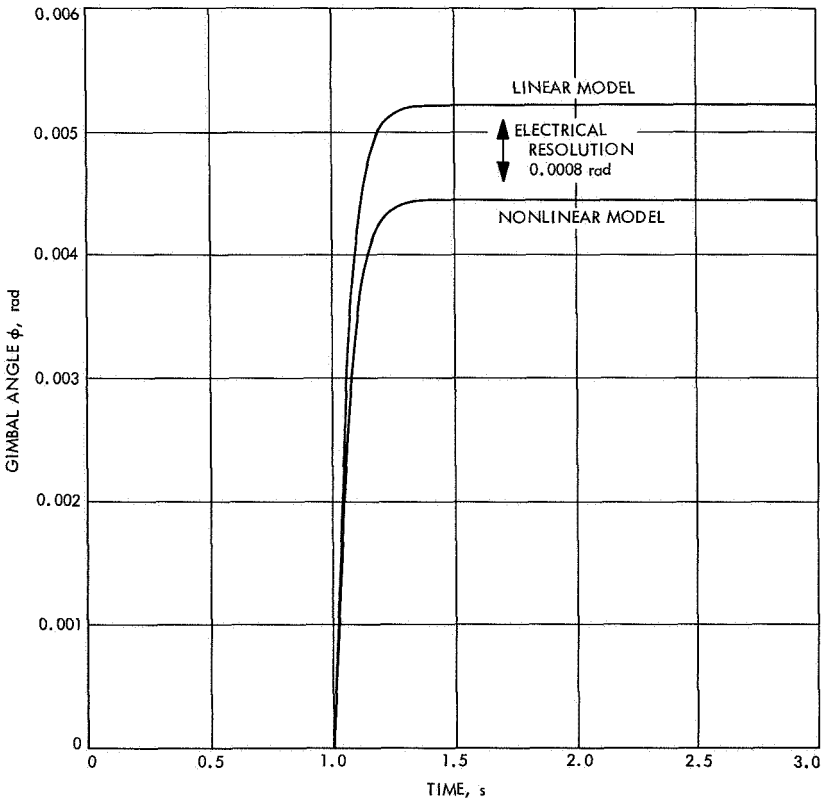

Fig. 29. Gimbal positions for both models

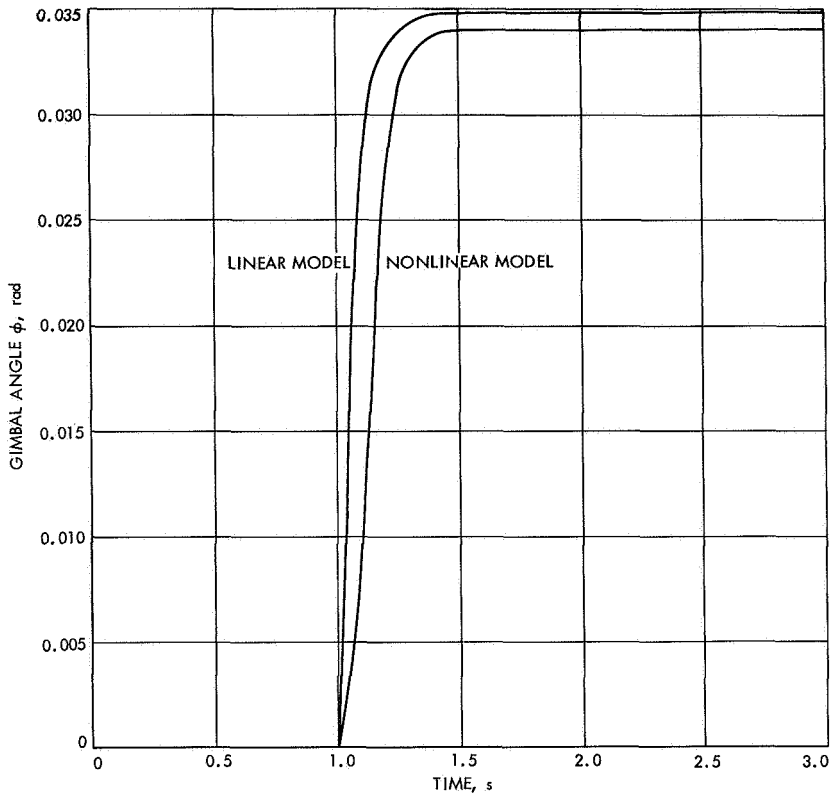

Fig. 30. Gimbal angle for both models

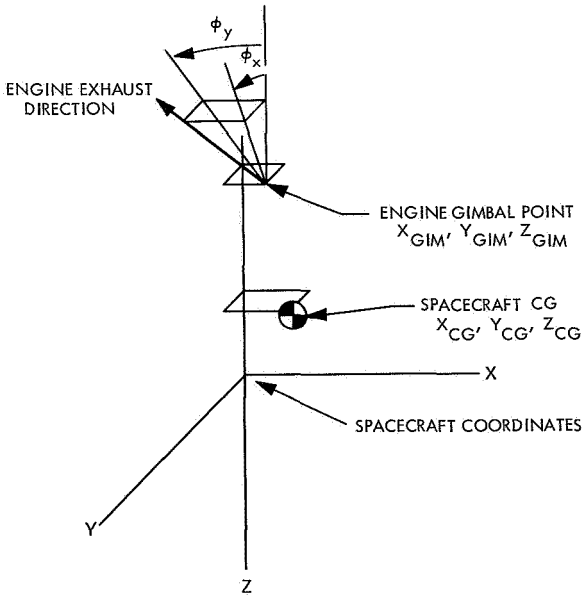

Fig. 31. Gimbal-angle definition

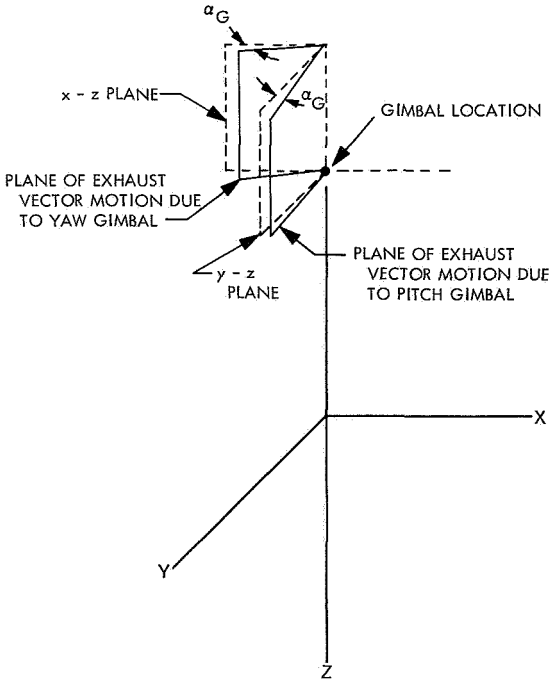

Fig. 32. *Mariner* orbiter engine mounting showing gimbal alignment error

both are treated as small angles. The CG is located at X_{CG}, Y_{CG}, and Z_{CG}, and the engine-gimbal point is at X_{GIM}, Y_{GIM}, Z_{GIM} in the spacecraft-coordinate system. If the engine-gimbal subassembly is allowed rotational alignment error as shown in Fig. 32, the equations for the engine force are

$$F_{Ex} = +T(\phi_y \cos \alpha_g - \phi_x \sin \alpha_g)$$
$$F_{Ey} = -T(\phi_x \cos \alpha_g + \phi_y \sin \alpha_g)$$
$$F_{Ez} = +T$$

If the following definitions are made:

$$d_1 \triangleq Z_{CG} - Z_{GIM}$$
$$d_2 \triangleq X_{CG} - X_{GIM}$$
$$d_3 \triangleq Y_{CG} - Y_{GIM}$$

the torque equations become

$$T_{Ex} = +d_1 F_{Ey} - d_3 F_{Ez}$$
$$T_{Ey} = -d_1 F_{Ex} + d_Z F_{Ez}$$
$$T_{Ez} = +d_3 F_{Ex} - d_2 F_{Ey} - T_S$$

where T_S is the swirl torque of the engine. If desired, other effects such as the alignment of the engine geometric axes to the actual thrust vector can be included in an approximate manner by adjusting X_{CG} and Y_{CG} appropriately.

2. Simplified equations. For use in a linearized analysis of this system the assumptions are made that α_g is zero and the gimbal point and the CG are in alignment in the XY plane. Then,

$$T_{Ex} = -d_1 T\phi_x$$
$$T_{Ey} = -d_1 T\phi_y$$
$$T_{Ez} = -T_S$$

IV. Autopilot Design and Constraints

A. Autopilot Design

The final system component to be designed is the autopilot. This is the circuit which receives signals from the gyro and uses them to command the gimbal servo. The system components which have been described thus far are relatively fixed and the autopilot is the only area in which the design is essentially free. With this in mind, the autopilot system under consideration is the result of several design attempts and iterations. This design is not considered optimal; however, this autopilot would be relatively simple to mechanize and would effectively control the vehicle during all the motor burns.

1. Basic circuit. The block diagram of the entire autopilot is shown in Fig. 33. There are three distinct functions which this system performs. The first and simplest function is that of limiting the output voltage to prevent driving the gimbal servo to the mechanical stops on the gimbal actuator. The 12-V level was selected because it is expected that this circuit will be realized using 15-V-operational amplifiers. For example, if a gimbal-servo scale factor of 1/3-deg/V is selected, the saturation in the autopilot will limit the gimbal travel starting at 4 deg. It is not expected that this limit would be reached under normal operating conditions in flight, but this protection would be useful during ground checkout.

The transient response of the autopilot system is controlled almost entirely by the forward path parameters K_D and T_F. To determine their numerical values it is necessary to neglect the effect of path guidance. Since it is not expected that the saturation limits will be reached, let the assumption be made that $K_P = 0$ and the autopilot transfer function is

$$G_a(S) = \frac{-K_D}{T_F S + 1}$$

Consistent with the previously developed models, the linearized pitch-axis autopilot system is represented in Fig. 34.

2. Spacecraft parameters. In order to analyze the loop presented in Fig. 34, it is necessary to know the numerical values of the various parameters. Obviously, any numbers used at this stage in the spacecraft configuration development will be very preliminary. They will be sufficiently close to the final values, however, to show the character of the system's performance. Thus, to illustrate the method of analysis and yaw selection for this study, these preliminary values will be treated as if they were values for a flight spacecraft.

One of the major factors in determining the character of the system response is the condition of the spacecraft. The letter "A" will be used to denote the condition when the spacecraft has a full complement of propellants

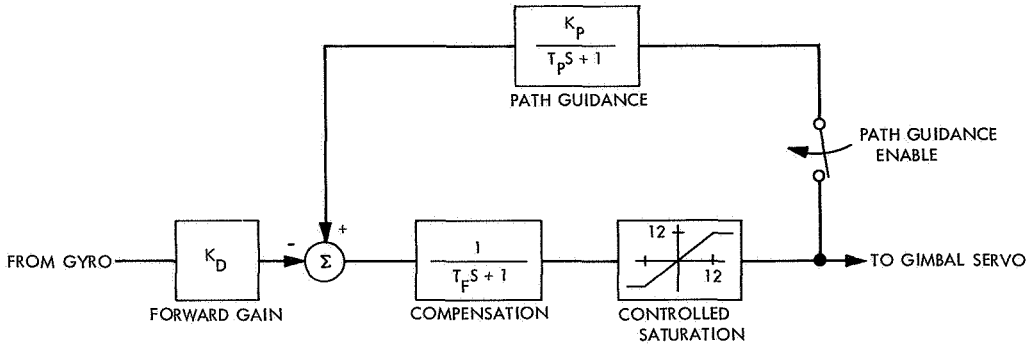

Fig. 33. Autopilot block diagram

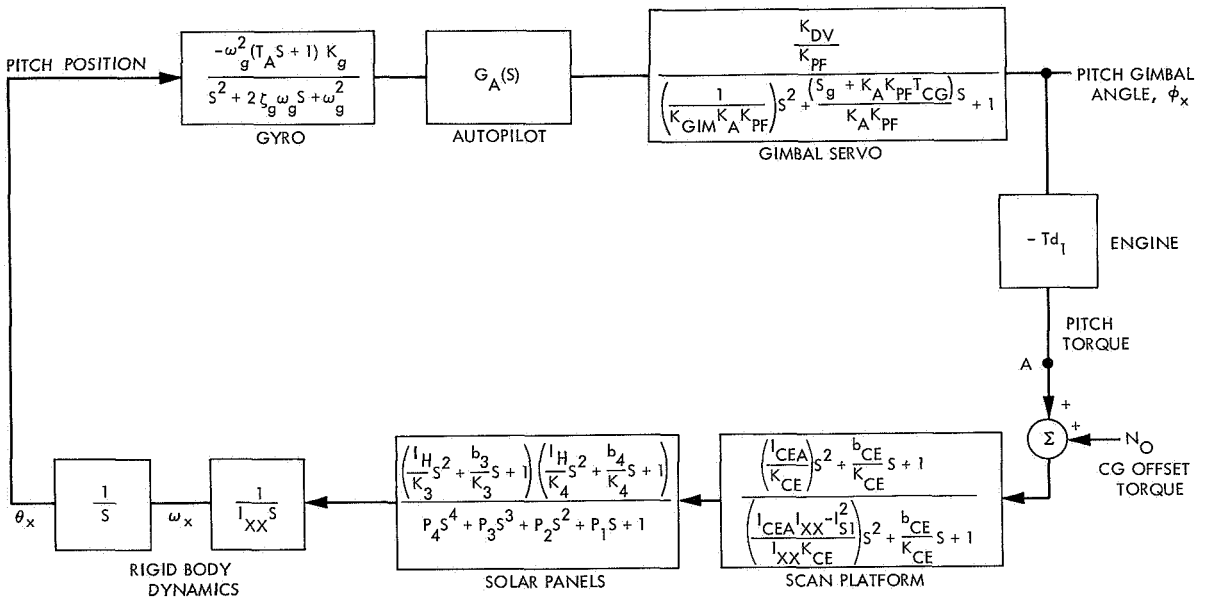

Fig. 34. Linearized and simplified pitch axis autopilot system

and the letter "B" will be used when all but the residuals have been consumed.

At this time the parameter values necessary to complete Fig. 34 will be computed from the values given in Tables 1 through 5. The basic engine-spacecraft parameters are

Parameter	Condition A	Condition B
Engine thrust, lb	300	300
Pitch moment of inertia, slug-ft²	278.5	233.3
Lever arm d_1, ft	2.21	2.957

For the scan platform the relevant parameters are

$Y_S = 0.361$ ft

$Z_S = 0.534$ ft

$Y_{CE} = -0.333$ ft

$Z_{CE} = 0.174$ ft

$\omega_{CE} = 33.5$ rad/s (conservative)

$\zeta_{CE} = 0.01$

$W_S = 180.21$ rad/s

$I_{CE} = 6.27$ slug-ft²

These yield the intermediate parameters

Parameter	Condition A	Condition B
L_{S1}, ft	0.361	–
L_{S2}, ft	0.694	–
L_{S3}, ft	0.36	–
L_{S4}, ft	2.204	1.457
I_{CEA}, slug-ft^2	9.69	–
I_{S1}, slug-ft^2	12.1	10.61

since

$$K_{CE} = I_{CEA}\,\omega_{CE}^2$$

and

$$b_{CE} = 2\,\zeta_{CE}\,\omega_{CE}\,I_{CEA}$$

The two models for the scan dynamics are

$$\frac{0.001979\,S^2 + 0.0008897\,S + 1}{0.00188\,S^2 + 0.0008897\,S + 1} \quad \text{condition A}$$

$$\frac{0.001979\,S^2 + 0.0008897\,S + 1}{0.00189\,S^2 + 0.0008897\,S + 1} \quad \text{condition B}$$

Table 9. Solar panel linear models for 10% panel matching

Case	Inertia	Frequency	Damping	Poles	Zeros
1	278.50	1.000	0.300	−2.977 − j7.313	−1.885 − j5.994
				−2.977 + j7.313	−1.885 + j5.994
				−2.022 − j6.185	−2.281 − j6.524
				−2.022 + j6.185	−2.281 + j6.524
2	278.50	1.000	0.700	−6.946 − j3.755	−4.398 − j4.487
				−6.946 + j3.755	−4.398 + j4.487
				−4.717 − j4.482	−5.322 − j4.410
				−4.717 + j4.482	−5.322 + j4.410
3	278.50	3.000	0.300	−8.931 − j21.940	−5.655 − j17.981
				−8.931 + j21.940	−5.655 + j17.981
				−6.065 + j18.555	−6.842 − j19.573
				−6.065 − j18.555	−6.842 + j19.573
4	278.50	3.000	0.700	−20.838 − j11.265	−13.195 − j13.461
				−20.838 + j11.265	−13.195 + j13.461
				−14.151 − j13.446	−15.966 − j13.230
				−14.151 + j13.446	−15.966 + j13.230
5	233.30	1.000	0.300	−3.213 − j7.548	−1.885 − j5.994
				−3.213 + j7.548	−1.885 + j5.994
				−2.030 − j6.197	−2.281 − j6.524
				−2.030 + j6.197	−2.281 + j6.524
6	233.30	1.000	0.700	−7.497 − j3.330	−4.398 − j4.487
				−7.497 + j3.330	−4.398 + j4.487
				−4.737 − j4.481	−5.322 − j4.410
				−4.737 + j4.481	−5.322 + j4.410
7	233.30	3.000	0.300	−9.639 − j22.643	−5.655 − j17.981
				−9.639 + j22.643	−5.655 + j17.981
				−6.091 − j18.590	−6.842 − j19.573
				−6.091 + j18.590	−6.842 + j19.573
8	233.30	3.000	0.700	−22.490 − j9.990	−13.195 − j13.461
				−22.490 + j9.990	−13.195 + j13.461
				−14.212 − j13.443	−15.966 − j13.230
				−14.212 + j13.443	−15.966 + j13.230

In factored form, these are

condition A

$$1.0526\,\frac{(S + 0.2248 + j22.478)\,(S + 0.2248 - j22.478)}{(S + 0.2366 + j23.06)\;\;(S + 0.2366 - j23.06)}$$

condition B

$$1.0471\,\frac{(S + 0.2248 + j22.478)\,(S + 0.2248 - j22.478)}{(S + 0.2354 + j23.0)\;\;(S + 0.2354 - j23.0)}$$

The situation is a little more complicated for the solar panels. It is assumed that the solar panels can have a bending-mode frequency ranging between 1 and 3 Hz with damping between 0.3 and 0.7. Matching of the bending modes can vary between panels. Both 10% and 25% panel matchings have been studied; for 10% matching, both the natural frequency and the damping factor of panel 2 are taken as 1.1 times those of panel 1. Similarly, the multiplier is 1.25 for the 25% matching. Four panel conditions were studied for both percentage matchings. These were 0.3 and 0.7 basic damping in combination with 1.0- and 3.0-Hz natural frequencies. The panel conditions were then examined for spacecraft conditions A and B, resulting in a total number of 16 combinations of 8 for each matching. The results for 10% matching are given in Table 9; the 25% case is shown in Table 10.

Table 10. Solar panel linear models for 25% panel matching

Case	Inertia	Frequency	Damping	Poles	Zeros
9	278.50	1.000	0.300	−3.689 − j7.979	−1.885 − j5.994
				−3.689 + j7.979	−1.885 + j5.994
				−2.106 − j6.299	−2.945 − j7.281
				−2.106 + j6.299	−2.945 + j7.281
10	278.50	1.000	0.700	−8.608 − j1.779	−4.398 − j4.487
				−8.608 + j1.779	−4.398 + j4.487
				−4.915 − j4.468	−6.872 − j3.802
				−4.915 + j4.468	−6.872 + j3.802
11	278.50	3.000	0.300	−11.068 − j23.936	−5.655 − j17.981
				−11.068 + j23.936	−5.655 + j17.981
				−6.319 − j18.897	−8.836 − j21.843
				−6.319 + j18.897	−8.836 + j21.843
12	278.50	3.000	0.700	−25.825 − j5.338	−13.195 − j13.461
				−25.825 + j5.338	−13.195 + j13.461
				−14.744 − j13.403	−20.617 − j11.407
				−14.744 + j13.403	−20.617 + j11.407
13	233.30	1.000	0.300	−3.943 − j8.188	−1.885 − j5.994
				−3.943 + j8.188	−1.885 + j5.994
				−2.136 − j6.338	−2.945 − j7.281
				−2.136 + j6.338	−2.945 + j7.281
14	233.30	1.000	0.700	−7.762 + j0.000	−4.398 − j4.487
				−10.641 + j0.000	−4.398 + j4.487
				−4.984 − j4.460	−6.872 − j3.802
				−4.984 + j4.460	−6.872 + j3.802
15	233.30	3.000	0.300	−11.830 − j24.563	−5.655 − j17.981
				−11.830 + j24.563	−5.655 + j17.981
				−6.408 − j19.015	−8.836 − j21.843
				−6.408 + j19.015	−8.836 + j21.843
16	233.30	3.000	0.700	−23.285 − j0.000	−13.195 − j13.461
				−31.923 + j0.000	−13.195 + j13.461
				−14.953 + j13.381	−20.617 − j11.407
				−14.953 − j13.381	−20.617 + j11.407

The approximations presented in Section III-B will be used for the gimbal servo model. Based upon the Autonetics P-106-A gimbal actuator, and a propellant line with a force of 20 ft-lb on the actuator, the important parameters are

$K_A = 1000$ V/mA

$K_{DV} = 0.1$ mA/V

$K_{PF} = 17.188$ mA/rad

$\omega_m = 0.0787$ rad/s

$T_m = 0.27$ s

$E_{SAT} = 28$ V

$E_T = 10$ V

$T_{FG} = 0.05$ s

Thus

$S_G = 228$ V/rad/s

$K_{GIM} = 0.01624$ rad/s²/V

This yields the transfer function

$$H(S) = \frac{0.005818}{0.00358\,S^2 + 0.063265\,S + 1}$$

or in factored form

$$H(S) = \frac{1.624}{(S + 8.83 + j14.183)(S + 8.83 - j14.183)}$$

The final system to be modeled is the gyroscope. There are two basic denominators for the gyro transfer function: a typical and a conservative denominator. In addition, R_1 and R_2 could be varied to change R_a and consequently the amount of lead compensation provided by the gyro which is represented by the time constant R_aC. Four models of the gyro were studied where the first model is the standard and the second is the conservative model. Models 3 and 4 represent changes from the traditional amount of lead compensation. The autopilot time constant, R_aC, was set at 2.5 s for model 3 and 1.0 s for model 4. The four models are as follows:

$$\frac{7744\,(1.77\,S + 1)\,K_G}{(S + 30.8 + j82.4)(S + 30.8 - j82.4)} \quad \text{gyro model 1}$$

$$\frac{2652.25\,(1.77\,S + 1)\,K_G}{(S + 12.41 + j50.0)(S + 12.41 - j50.0)} \quad \text{gyro model 2}$$

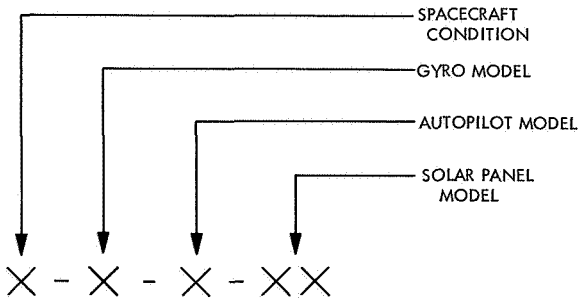

Fig. 35. Identifier system

$$\frac{7744\,(2.5\,S + 1)\,K_G}{(S + 30.8 + j82.4)(S + 30.8 - j82.4)} \quad \text{gyro model 3}$$

$$\frac{7744\,(1.0\,S + 1)\,K_G}{(S + 30.8 + j82.4)(S + 30.8 - j82.4)} \quad \text{gyro model 4}$$

All the parameters necessary for an analysis of the block diagram shown in Fig. 34 are now known.

3. Reference Bode plots. In order to systematically operate with the various alternate models presented in the previous section, a coding system was devised. Each configuration of the autopilot system was represented by an identifier. The manner in which the identifier is constructed is illustrated in Fig. 35. For example, B-2-1-08 would refer to the autopilot system where the conservative gyro model was being considered with the spacecraft in condition B. The solar panels are matched to 10% with natural frequency of 3.0 Hz and damping factor of 0.7. The autopilot circuit model is model 1 which is the only model thus far considered

$$G_A(S) = \frac{-K_D}{T_F\,S + 1}$$

with T_F taken as 1/9 s. Other autopilot models will be discussed as the analysis is presented. The reasons for the selection of the 1/9-s value for the filter time constant are that the 1.43-Hz break frequency provides reduction of the gyro noise and the 12 dB roll-off at 6 Hz decouples the system from the scan platform dynamics.

The autopilot will now be analyzed using Bode plots with two systems used more or less as reference configurations. These are A-1-1-01 for spacecraft condition A and B-1-1-05 for spacecraft condition B. Their Bode plots are presented in Figs. 36–39. On the magnitude plots the points of 180-deg phase are marked, and these show that for A-1-1-01 the critical gain is 16 dB and for B-1-1-05 it is 15.5 dB.

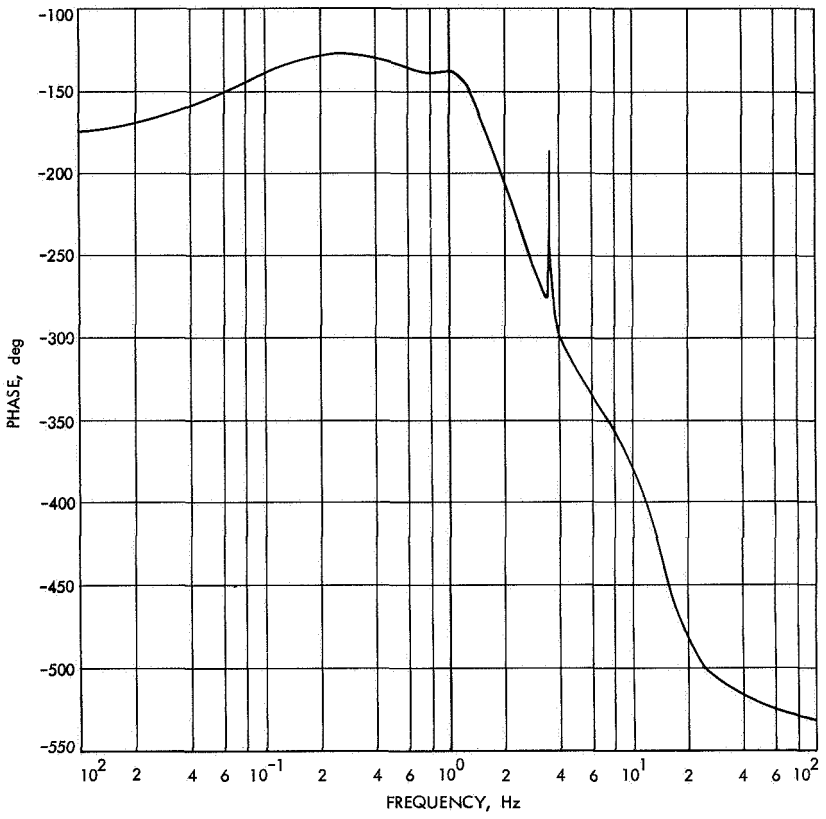

Fig. 36. Bode plot A-1-1-01, phase vs frequency

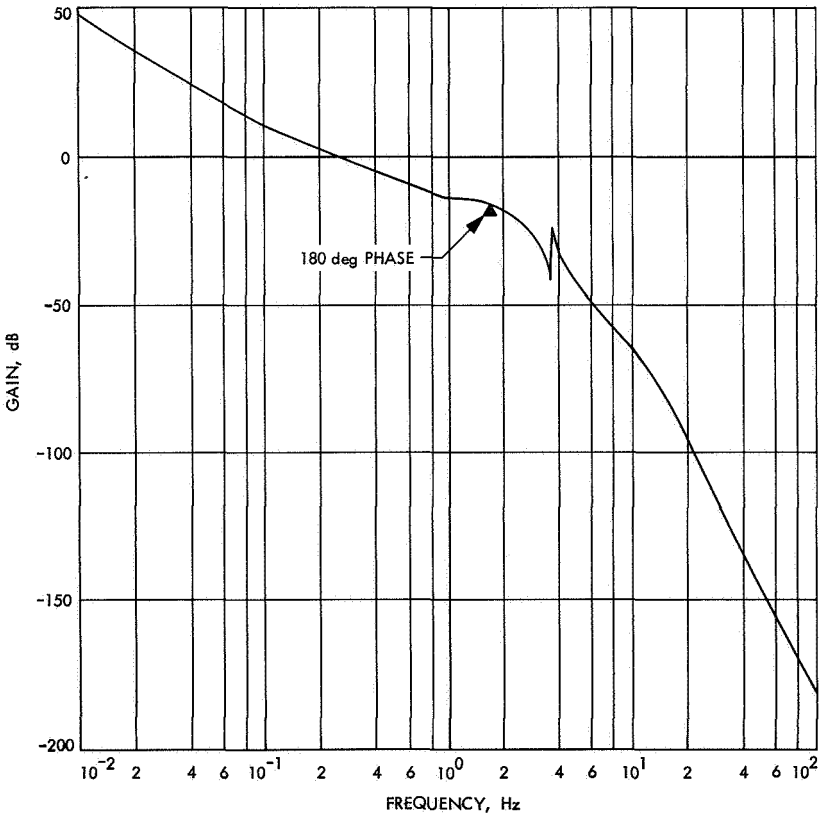

Fig. 37. Bode plot A-1-1-01, gain vs frequency

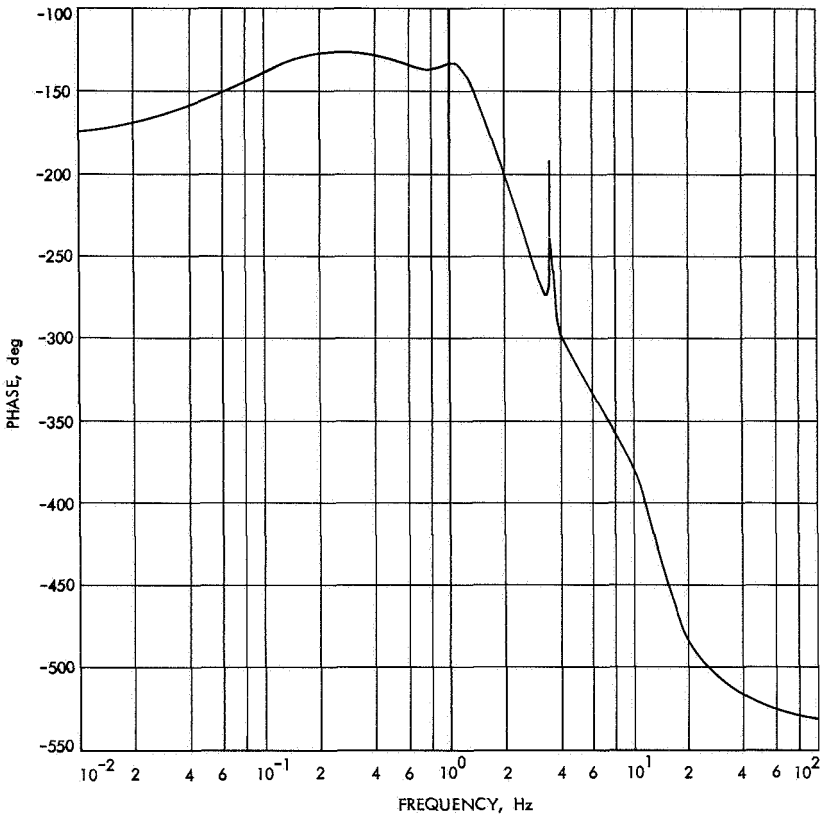

Fig. 38. Bode plot B-1-1-05, phase vs frequency

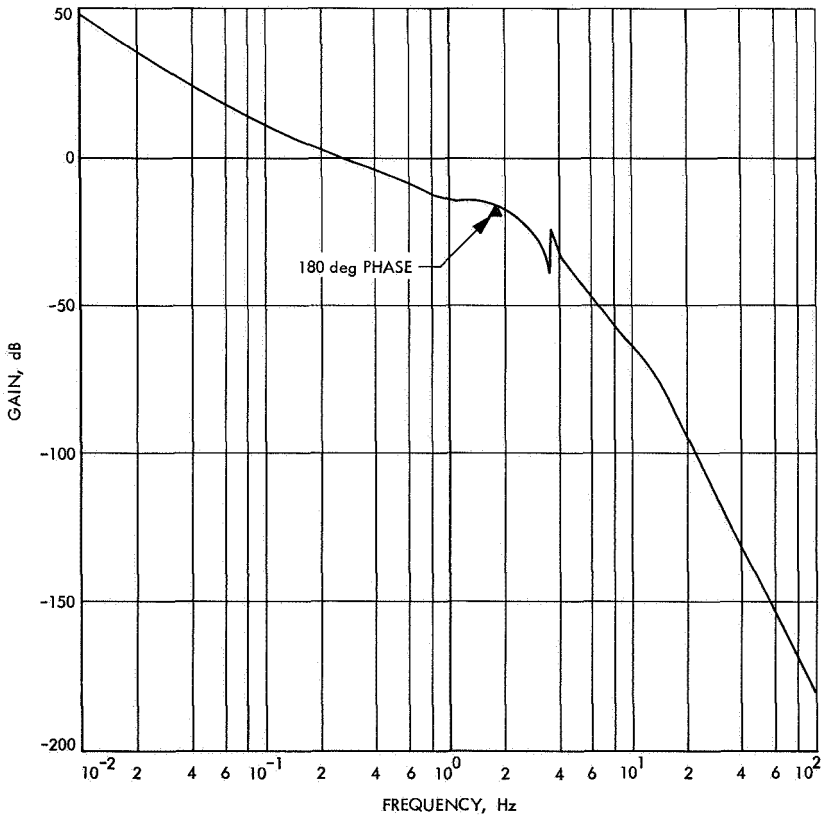

Fig. 39. Bode plot B-1-1-05, gain vs frequency

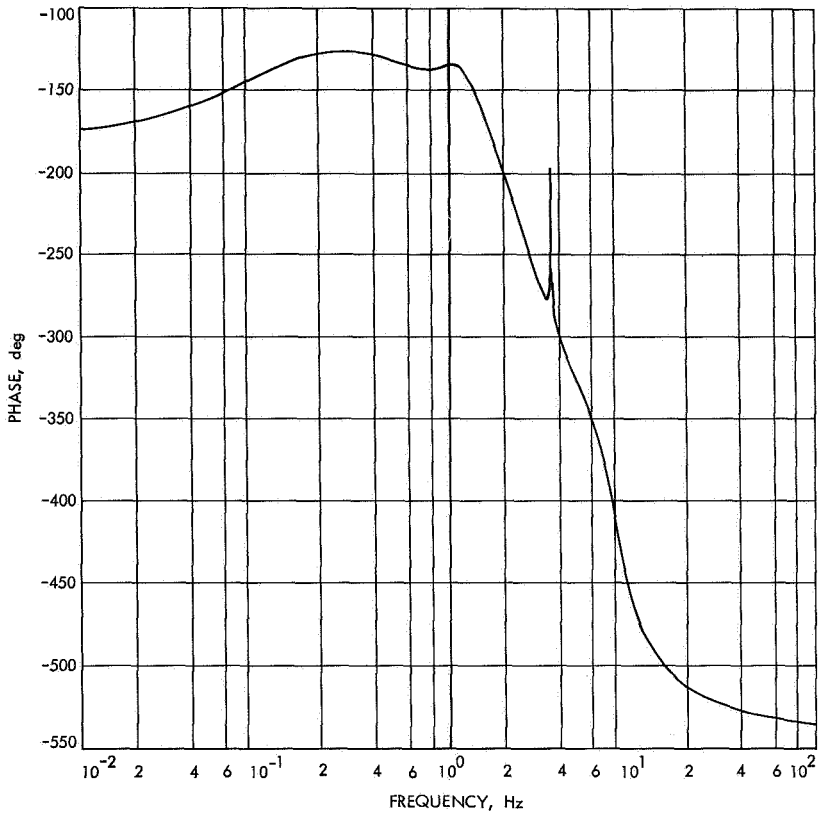

Fig. 40. Bode plot B-2-1-05, phase vs frequency

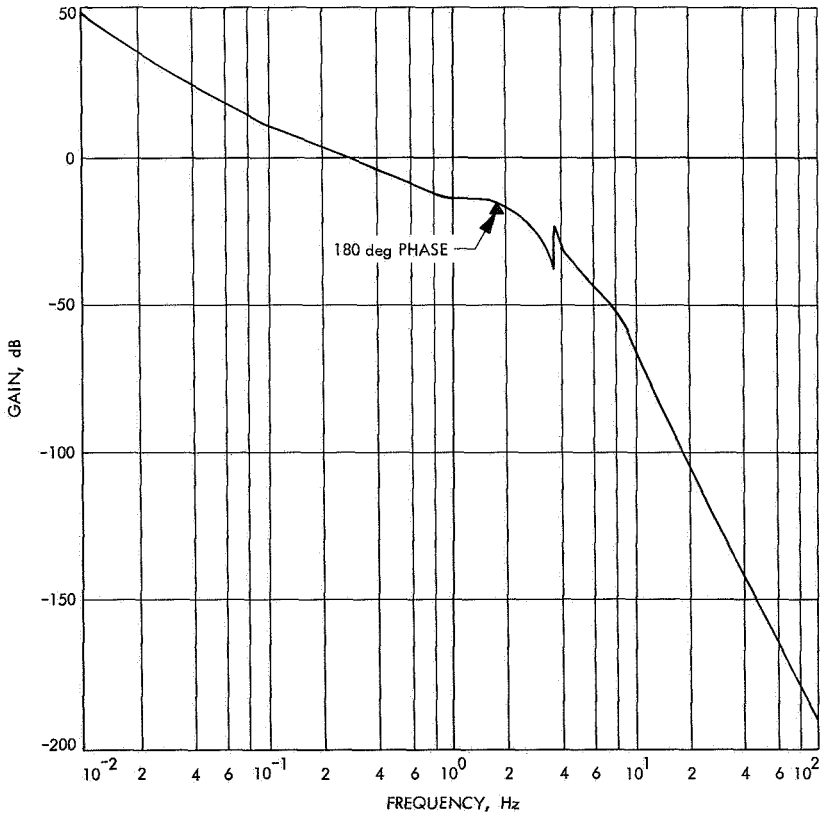

Fig. 41. Bode plot B-2-1-05, gain vs frequency

To investigate the effect of raising the solar panel frequency and simultaneously increasing the damping, cases A-1-1-04 and B-1-1-08 were run with the resulting critical gains of 16 dB and 17 dB, respectively. Thus, for rotational stability the panel frequencies and dampings are not critical. Panel matching was considered with case B-1-1-13 with a 25% matched condition. The resulting critical gain was 16 dB. When the conservative gyro model was used, little effect was noted with a critical gain of 14.5 dB for B-2-1-05 as shown in Figs. 40 and 41.

Final investigation was made on the location of the gyro zero or the rate compensation. Increasing the rate damping of the loop with case B-3-1-05 resulted in a degraded situation with a critical gain of 13 dB. Decreasing the damping with B-4-1-05 improved the situation slightly with 19 dB, but the extra gain was determined not worth the effort in changing the padded torquer resistance from the *Mariner* Mars 1969 value. The Bode plots are summarized in Table 11.

4. Gain selection. Case B-1-1-05 was considered typical and was used to determine the gain level of the system. The closed-loop step response of B-1-1-05 for various gains from −5 dB to +15 dB is shown in Fig. 42. As demonstrated in Fig. 42(f), 15 dB is very close to the critical gain. In the actual system, the loop Bode gain is given by

$$K = \frac{K_G K_D K_A T d_1}{I_{XX}}$$

where

K_G = gyro position scale factor

K_D = autopilot circuit forward gain

K_A = gimbal servo gain; K_{DV}/K_{PF}

T = engine thrust

d_1 = lever arm

I_{XX} = moment of inertia

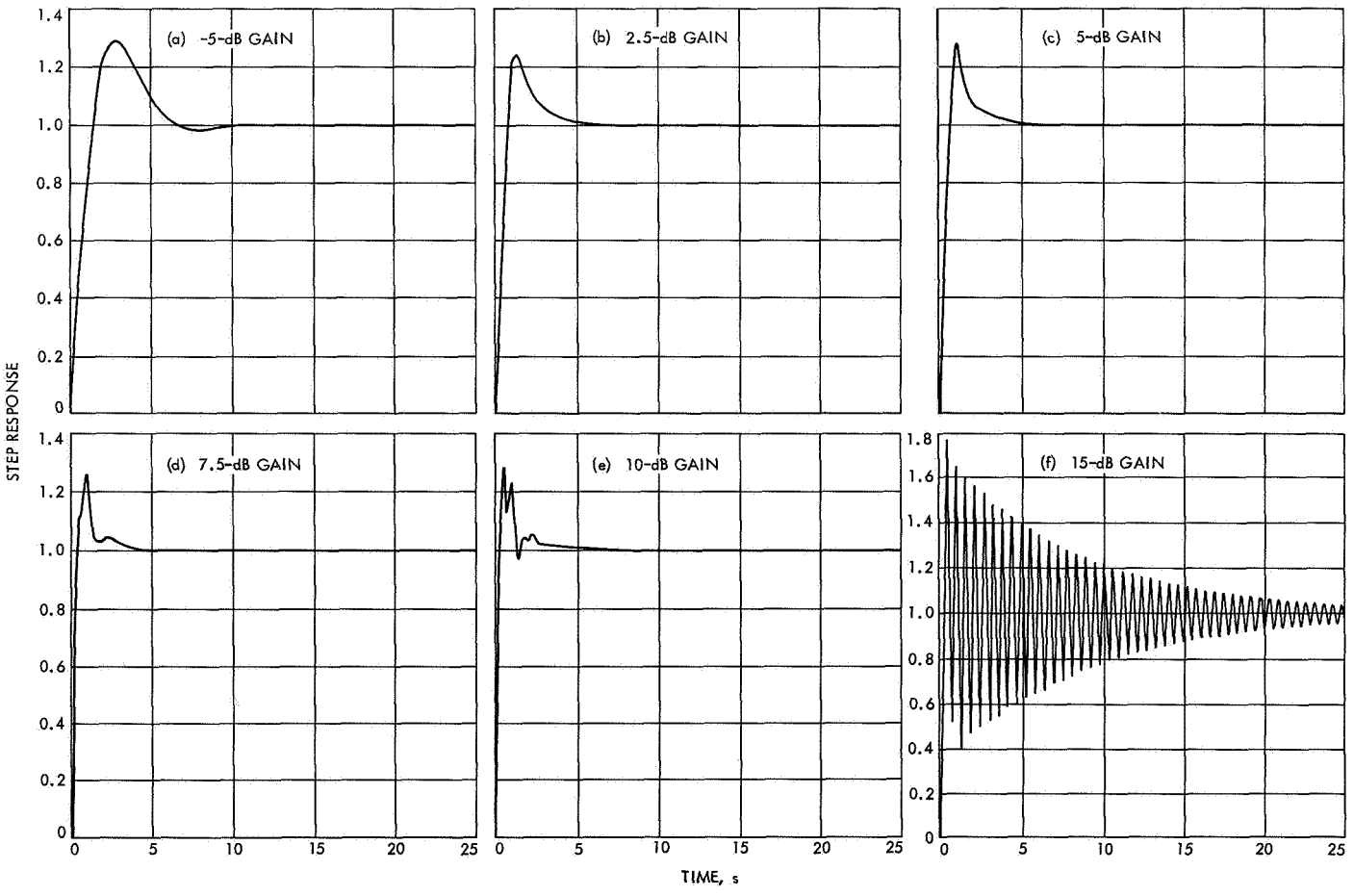

Fig. 42. Closed loop response B-1-1-05 with 15-dB gain

Table 11. Bode plot summary

Case	Magnitude, dB (180 deg phase)
A-1-1-01	−16
B-1-1-05	−15.5
A-1-1-04	−16
B-1-1-08	−17
B-1-1-13	−16
B-2-1-05	−14.5
B-3-1-05	−13
B-4-1-05	−19

It is important to determine the accuracy and variation of these values. It was determined, earlier in this report, that the gyro scale factor could have a 2.5% variation with temperature. In addition, there is a 1.0% measurement repeatability and an estimated 2.0% accuracy for the technique. Thus, the worst-case error for K_G is 5.5%. The gimbal servo will have approximately 3.0% linearity, and the moment of inertia at the extremes of propellant loading is accurate to 15%. Further, the product of the CG-engine lever arm multiplied by the engine thrust, Td_1, is also a 15% value. In summation,

$$K_G = 166.16 \pm 5.5\%$$

$$K_A = 0.005818 \pm 3\%$$

$$I_{XX} = 278.5 \text{ and } 233.5 \pm 15\%$$

$$Td_1 = (300)(2.21) \text{ and } (300)(2.957) \pm 15\%$$

resulting in the nominal gains

$$K = 2.3014\, K_D \quad \text{condition A}$$

$$K = 3.676\, K_D \quad \text{condition B}$$

The accuracies are summed in a worst-case manner to yield 38.5% variation. Thus, the low and high extremes of gain are

$$K = 1.415\, K_D \quad \text{condition A, worst case}$$

$$K = 5.091\, K_D \quad \text{condition B, worst case}$$

Since

$$20 \log \frac{5.091}{3.676} = 3 \text{ dB}$$

a 3-dB pad is necessary to handle worst-case gain variations.

It was determined that under no circumstance would more than 10 dB of gain be used. This would still yield an acceptable step response as shown in Fig. 43. After subtracting the 3-dB pad for worst-case gain variations, the nominal high-gain point is 7 dB. Thus,

$$20 \log 3.676\, K_D = 7 \text{ dB}$$

where

$$K_D = 0.61$$

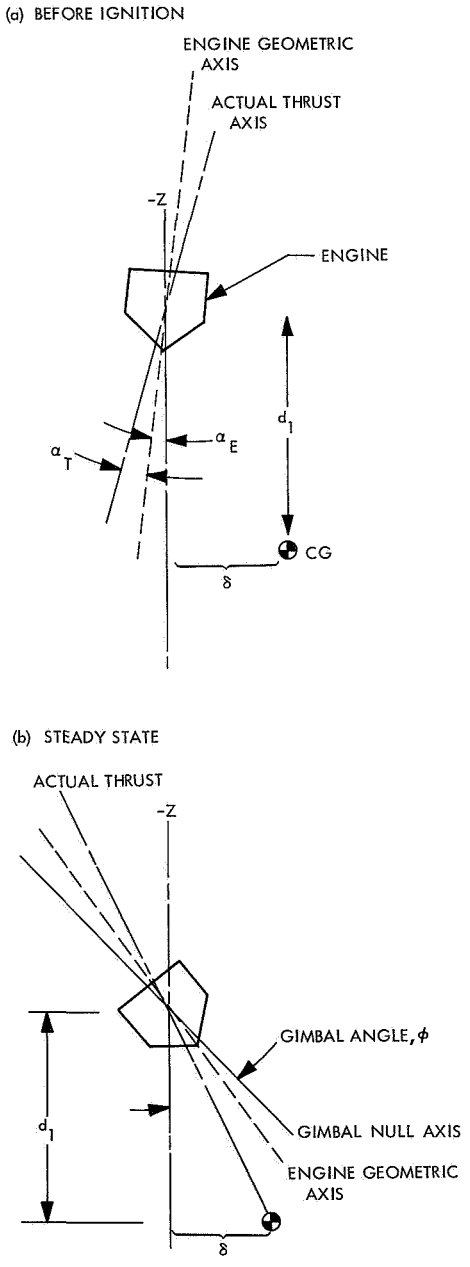

Fig. 43. Closed loop response for B-1-2-05

With this value of autopilot forward gain, the gain at condition B would be the 7 dB and the system would exhibit a step response similar to Fig. 44. The gain at condition A would be nominally

$$20 \log (2.3014)\,(0.61) = 3 \text{ dB}$$

with approximately the response shown in Fig. 45.

5. Basic-system steady-state error. The accuracy of the basic autopilot is not high. This is because the gain K_F between the gyro input and gimbal angle is low. The single-axis representation in Fig. 45 shows three mechanical errors: δ is the CG offset, α_T is the angular error between the actual thrust and the engine geometric-thrust axis, and α_E is the engine angular-alignment error. During steady-state operation, the actual thrust is through the CG; therefore, there is an angular error between the spacecraft Z axis and the actual thrust of δ/d_1 rad. Furthermore, there is the angle through which the spacecraft must rotate to produce enough gyro output to drive the gimbal to the angle ϕ. Thus,

$$K_G\, K_D\, K_A\, \theta = \phi = \alpha_T + \alpha_E + \frac{\delta}{d_1}$$

The total steady-state thrust vector error is

$$\alpha_S = \theta + \frac{\delta}{d_1} = \frac{1}{K_F}(\alpha_T + \alpha_E) + \frac{K_F + 1}{K_F}\left(\frac{\delta}{d_1}\right)$$

where $K_F = K_G\, K_D\, K_A$. Using $K_D = 0.61$ as determined in the previous section,

$$K_F = 0.5897$$

and

$$\alpha_S = 1.7\,(\alpha_T + \alpha_E) + 2.7\,(\delta/d_1)$$

Assuming the errors given in Table 4,

$$\alpha_S \text{ (worst case)} = 5.77 \text{ deg}$$

at first midcourse correction.

6. Path guidance gain. When the spacecraft is at a steady-state condition during motor burn, the engine is aimed at the CG and makes an angle ϕ with the spacecraft Z axis. Since this angle is commanded by the autopilot, it is a known source of thrust-vector error. The purpose for path guidance is to correct for this error by the simple method of setting the steady-state gain between gyro input and gimbal angle equal to -1. For stability, the gimbal has to point the engine through the CG; thus, the attitude angle of the spacecraft must be the negative of the gimbal angle. Therefore, in theory, the thrust vector will be exactly in the inertial reference direction.

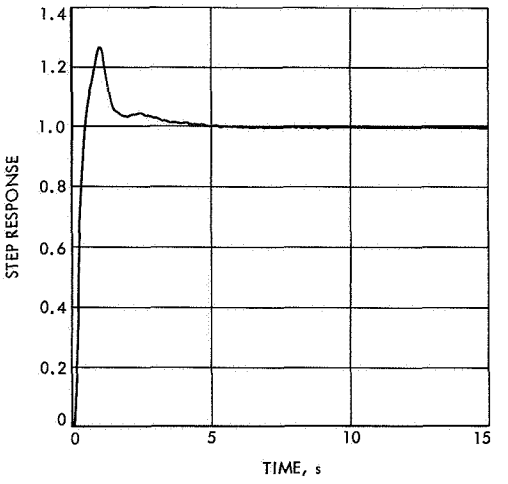

Fig. 44. Closed loop response for B-1-6-05

From the complete autopilot loop of Fig. 33, it can be seen that the path-guidance feedback is used to modify the steady-state gain. There is an associated lag T_P which is used to prevent this feedback from degrading the transient performance of the system.

The feedback K_P is easily set by the relation

$$K_P = 1 + K_F$$

where

$$K_F = K_G\, K_D\, K_A$$

with

K_G = gyro scale factor

K_D = forward gain

K_A = gimbal servo gain K_{DV}/K_{PF}

This yields the steady-state error

$$K_F\, \theta + K_P\, \phi = \phi = \alpha_T + \alpha_E + \frac{\delta}{d_1}$$

if K_P were exactly its nominal value,

$$\alpha_S = -\alpha_T - \alpha_E$$

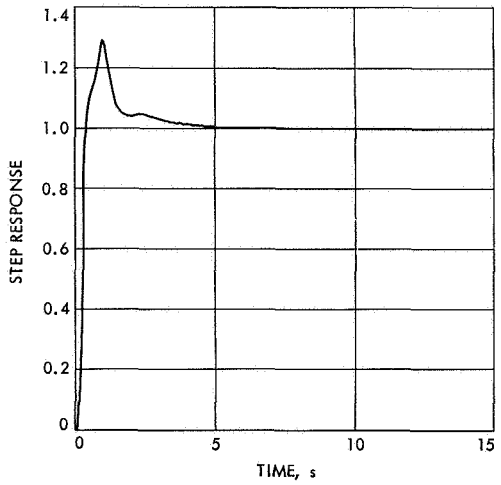

Fig. 45. Basic system steady-state error

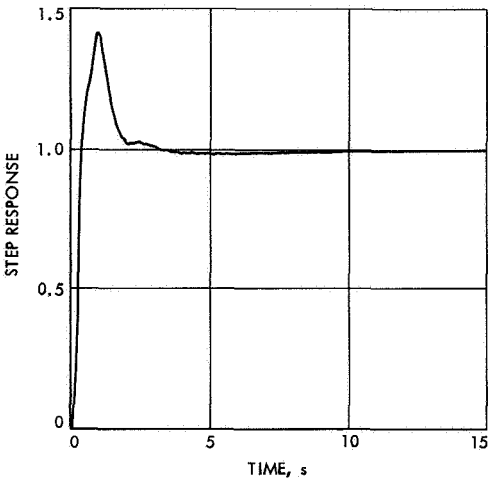

Fig. 46. Closed loop response B-1-1-05 with 7-dB gain

Because of the thermal variations in K_G and the gimbal-servo linearity, the steady-state thrust-vector error is approximated by

$$\alpha_S \approx -\alpha_T - \alpha_E + (\Delta K_F/K_F)\left(\frac{\delta}{d_1}\right)$$

where $\Delta K_F/K_F$ is approximately 0.10 (worst case) and 0.063 (3 σ). A comparison of steady-state thrust-vector errors for the autopilot with and without path guidance is presented below.

	Worst case	3 σ
Without path guidance, deg	5.77	3.7
With path guidance, deg	1.26	0.72

7. Path-guidance time constant. The path-guidance time constant must be selected to be as short as possible without seriously degrading the transient performance. The shorter the time constant, the sooner the system will compensate for the gimbal pointing angle. With this object in mind, five autopilot circuits with path guidance were investigated and given the identifier codes 2 through 6. These were for a path-guidance gain of 1.5897 and time constants of 3, 5, 10, 15, and 20 s. The overall autopilot-circuit transfer functions are given in Table 12. The value of K_D for proper transient response has already been set at 0.61 and this value has been used in computing K_P. Thus, the open-loop gain for autopilots 2 through 6 is

$$K = (-1)\left(\frac{Td_1}{I_{XX}}\right)$$

which is calculated to be −2.3806 for spacecraft condition A and −3.8024 for condition B. In judging transient response, autopilot circuit 1 without path guidance will be used as a standard. In Section IV-A-4 the value $K_D = 0.61$ was computed to give a 7-dB open-loop gain at condition B. Thus, the standard step response will be B-1-1-05 with a 7-dB loop gain. This response is shown in Fig. 46.

In Fig. 44 the response for the 20-s path-guidance loop is plotted; as can be seen, this circuit has only slightly more overshoot. Decreasing the path-guidance time constant to 3 s did increase the overshoot substantially, as shown in Fig. 43. A plot of overshoot as a function of path-guidance time constant is shown in Fig. 47. From

Table 12. Autopilot circuit summary

Autopilot model	K_P	T_P	Transfer function
1	0	—	$0.61\,\frac{9}{S+9}$
2	1.5897	3	$K_D\,\frac{9\,(S+0.333)}{(S-0.1858)\,(S+9.519)}$
3	1.5897	5	$\frac{9\,(S+0.2)}{(S-0.11396)\,(S+9.314)}$
4	1.5897	10	$\frac{9\,(S+0.1)}{(S-0.058)\,(S+9.158)}$
5	1.5897	15	$\frac{9\,(S+0.0667)}{(S-0.03886)\,(S+9.1055)}$
6	1.5897	20	$\frac{9\,(S+0.05)}{(S-0.0292)\,(S+9.079)}$

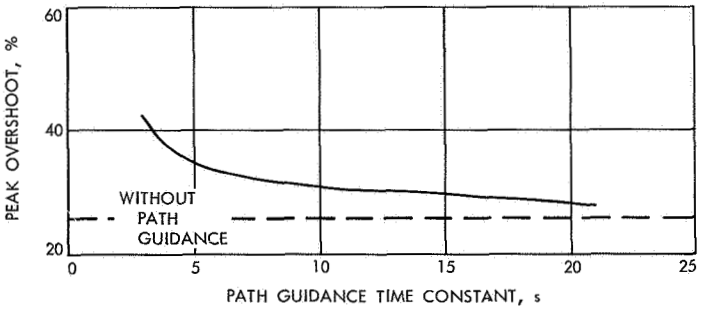

Fig. 47. *Mariner* orbiter autopilot, orbit trim

this plot, the value of 5 s was selected as a good compromise between overshoot and path-guidance response time. For spacecraft condition A, the response of A-1-3-01 was checked against A-1-1-01 with 3-dB gain; the overshoot increase was found to be approximately the same as for condition B.

8. Secondary effects of path guidance. There are two secondary effects of path guidance on the system. The first effect is to introduce a lower gain limit. If system gain falls below this value, a low frequency instability will result. Figs. 48 and 49 show the open-loop Bode plots for the 5-s path-guidance autopilot circuit. The critical gains marked on Fig. 48 are well outside the operating limits, and the low gains limit the cycle frequency. The dead space in the gimbal servo acts as a variable gain for sinusoidal inputs. This system will oscillate at low frequency under normal operation. The magnitude of these oscillations is set by E_T and the gimbal-servo loop gains. The effect of path guidance is to raise this limit-cycle frequency so that the period is approximately equal to T_P without changing the magnitude. The overall effect on the system is negligible.

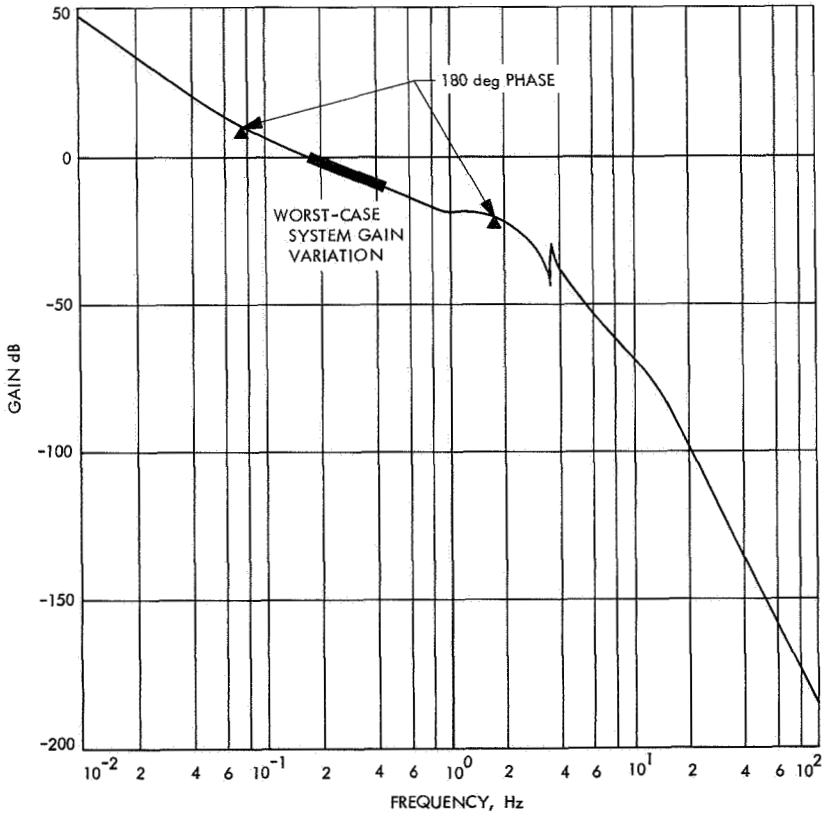

Fig. 48. Bode plot B-1-3-05, gain vs frequency

B. Autopilot-Imposed Constraints on the Spacecraft

During the transient response of the autopilot following engine ignition, the spacecraft can attain relatively high angular rates. The autopilot system is limited in the magnitude of angular rate it can tolerate, due to gyro saturation, and this fact imposes constraints on the overall spacecraft design. The mechanism of gyro saturation can be seen in Fig. 11. The dc gyro-rebalance amplifier is limited to about ±31 V maximum output and this, in turn, limits the current which can be pushed through the torquer. Once saturation occurs, the gimbal is no longer captured. Since V_G starts near zero and changes very slowly, the approximate maximum rate for the system is

$$\dot{\theta}_{MAX} \approx \frac{K_T V_{SAT}}{H (R_1 + R_2 + R_T)}$$

where K_T and H are set by the gyro selection, and $R_2 + R_T$ is set by the autopilot system rate to position time constant of 1.77 s. Thus,

$$\dot{\theta}_{MAX} \approx \frac{0.07777\, V_{SAT}}{R_1 + 0.4}, \text{ deg/s}$$

where R_1 is in kilohms. The term V_{SAT} cannot be increased from its present value without requiring higher voltage capacitors, high-voltage transistors, and possibly corona protection since the gyros run during launch. This leaves only R_1 as the controlling factor; R_1 should be reduced for this mission from its traditional value of 845 ohms to 100 ohms.

1. Solar panel constraints. It has been established that coupling exists between the vehicle's translation and solar panel flexure. This is evidenced by the appearance of $\ddot{Z}$ terms in the hinge-bending equations. In order not to introduce peak oscillatory rates into the spacecraft, the solar panels on the spacecraft axis must be matched. An experimentally determined set of constraints has been developed. Panels on the same axis must be matched to 2% in mass moment, 10% in damping factor, and 10% in undamped natural frequency. The mass moment is defined as the product of a panel's mass and the distance from the hinge line to its CG. In addition to this, no panel may have an undamped natural frequency less than 1.0 Hz nor a damping factor outside of the range 0.3 to 0.7.

2. CG offset. The offset between the gimbal at null-thrust vector and the actual CG location is the most important factor in determining peak gyro voltage. When ignition occurs the engine thrust is essentially a step function of force, since its time constant is extremely short when compared with that of the rest of the system. It can be seen (Fig. 45) that this thrust acts through the lever arm ℓ, where

$$\ell = S + d_1 (\alpha_E + \alpha_T)$$

This torque introduces a body rate into the spacecraft which is sensed by the gyros. Within an extremely brief period of time this error signal is large enough to completely saturate the gimbal-servo power amplifier and full voltage is applied to the motor. The gimbal system now begins slowing the thrust over toward the CG location with the approximate gimbal angle given by

$$\phi = \omega_m t - T_m \omega_m \left(1 - \varepsilon^{-t/T_m}\right)$$

where

ω_m = maximum gimbal rate

T_m = gimbal-actuator time constant

Thus, if the CG offset were ℓ_0, the angle the gimbal would have to move is

$$\phi_0 = \frac{\ell_0}{d_1}$$

The preceding equation for ϕ could then be solved implicitly for the time $\hat{t}$ it takes to move the required angle ϕ. However, the entire time the gimbal is slowing, the body angular rate is increasing as given by

$$\omega = \frac{T d_1}{I_{XX}} \times \left[(\phi_0 + T_m \omega_m)\, t - \frac{1}{2} \omega_m t^2 - T_m^2 \omega_m \left(1 - \varepsilon^{-t/T_m}\right) \right]$$

and the peak is reached when the gimbal reaches ϕ_0 at time $\hat{t}$. Substituting into the above relation yields the peak rate $\hat{\omega}$. Since the gyros are most sensitive to rate and since little error can accrue in this brief period, the equivalent gyro output (Fig. 15) at the rebalance amplifier is

$$V'_G = K_G T_G \hat{\omega}$$

where

K_G = position scale factor

T_G = rate to position time constant $(R_1 + R_2 + R_T)\, C$

In addition, there is the rate induced by the unmatched solar panels. This is approximately 5.2 mrad/s, and produces an equivalent gyro output

$$V''_G = 0.0052\, K_G\, T_G$$

The final factor to be considered is the character of the system response. From Fig. 49, it can be seen that the system has a 35% overshoot when the path-guidance time constant is 5 s. Combining all these factors, the total estimated peak gyro voltage is

$$V_G\,(\text{peak}) = 1.35\,(V'_G + V''_G)$$

This peak voltage is plotted in Fig. 50 versus CG offset for the traditional 845-ohm value for R_1 and the proposed value of 100 ohms. This plot demonstrates the total CG offset limits which must be observed.

*3. **Roll axis attitude control.*** Since the roll axis is to be stabilized during the motor burns by the attitude-control cold-gas system, it is important to estimate the torques the engine will produce due to swirling of the exhaust gases. There is a rule of thumb for engines which predicts the practical level for swirl-torque measurement. This relation is

$$T_S = 0.001\, TR$$

where

T_S = swirl torque, lb-ft
T = engine thrust, lb
R = nozzle exit radius, ft

For the RS-1401 engine with an expansion ratio of 40 to 1, the predicted value would be 0.108 lb-ft. From the experience of *Lunar Orbiter* the values from the above equation would seem to be extremely conservative. Unfortunately, this fact is of little consequence because it would be prohibitively expensive to test each engine to very low torque levels. It has been estimated that an economic level for testing this engine would be 2 in.-lb. This is equivalent to 0.167 lb-ft, which is close to the value predicted by the rule of thumb. This means that if

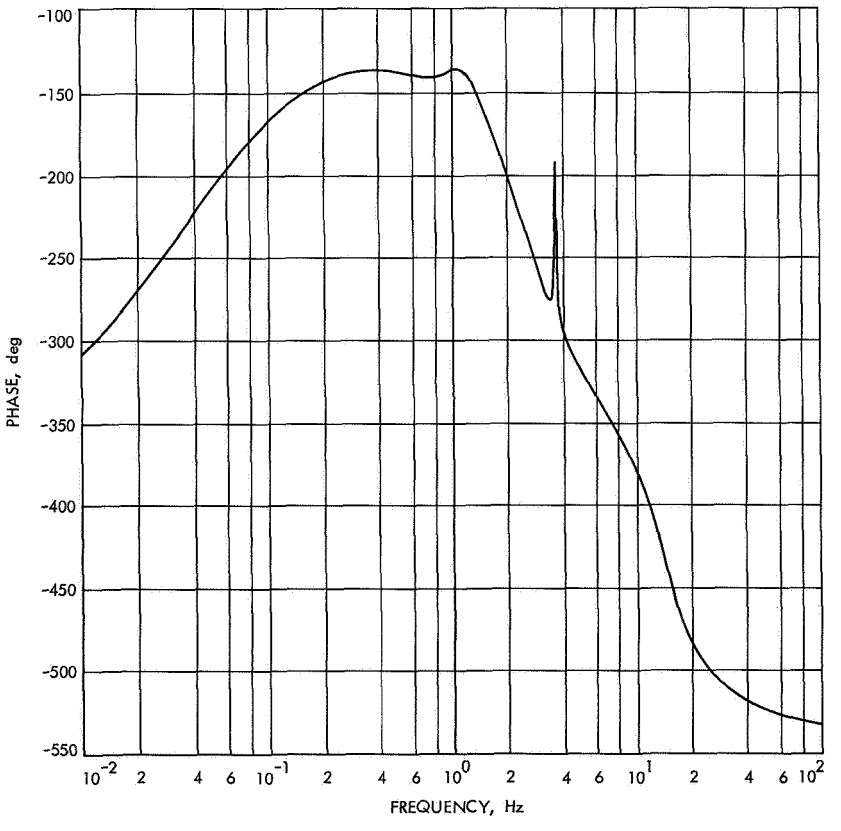

Fig. 49. Bode plot B-1-3-05, phase vs frequency

there is no special mode for roll-axis control during motor burns, the regular attitude-control jets will be sized by this requirement.

The roll-control system must be able to maintain control in the event of a half-gas system failure; this requires each one of the roll jets to be sized at 0.167 lb-ft. If the standard acceleration constant of 0.45×10^{-3} rad/s^2 were employed during cruise, this would size each jet at 0.082 lb-ft. The increase in jet sizing will increase half-gas system consumption for limit-cycle operation by only 0.2 lb of nitrogen. This excludes leakage, which is the major factor in gas consumption. The only alternative is to place additional roll jets on the spacecraft which are switched on to provide a higher torque level during motor burns. This is undesirable for three reasons: (1) the extra jets would raise the gas leakage and require storing approximately ⅓ more N_2, (2) it would increase the possibility of a valve-open type failure, and (3) the auxiliary valves would not be operated during the long cruise period and, thus, there is a possibility of cold-vacuum welding taking place in the valve. The recommended method for roll control during burns is, therefore, to increase the thrust of each of the normal roll jets to approximately 17.5 mlb. This will make it possible for either jet alone to combat swirl torque during burns. The only possible problem with this method is that 17.5 mlb might be near the limit for *Mariner* Mars 1969 valves and the stroke of the valve might have to have a minimum value specified to ensure obtaining this thrust level.

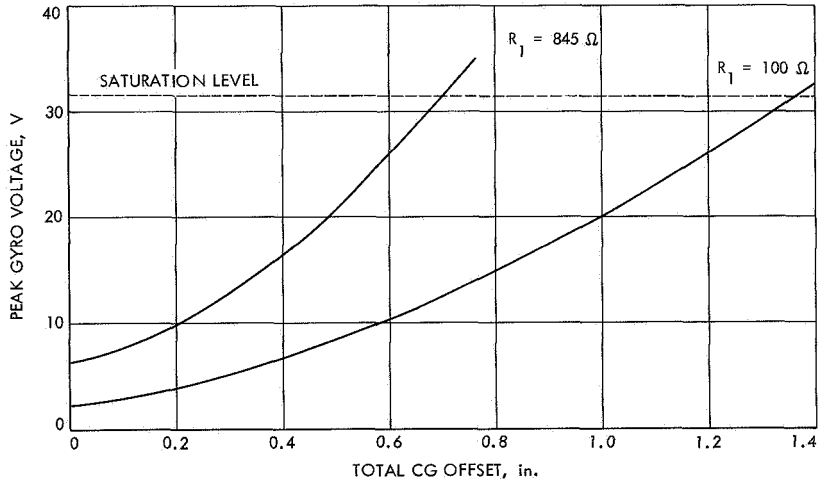

Fig. 50. *Mariner* orbiter gyro overshoot as a function of series resistor R_1

Appendix A

Autopilot Mechanization

A possible autopilot circuit (Fig. A-1) has been designed and a breadboard has been tested. The preliminary results indicate that this would be a good starting place for a flight autopilot design. The resistors R1, R2, and R3 should be made available for gain and balance adjustments.

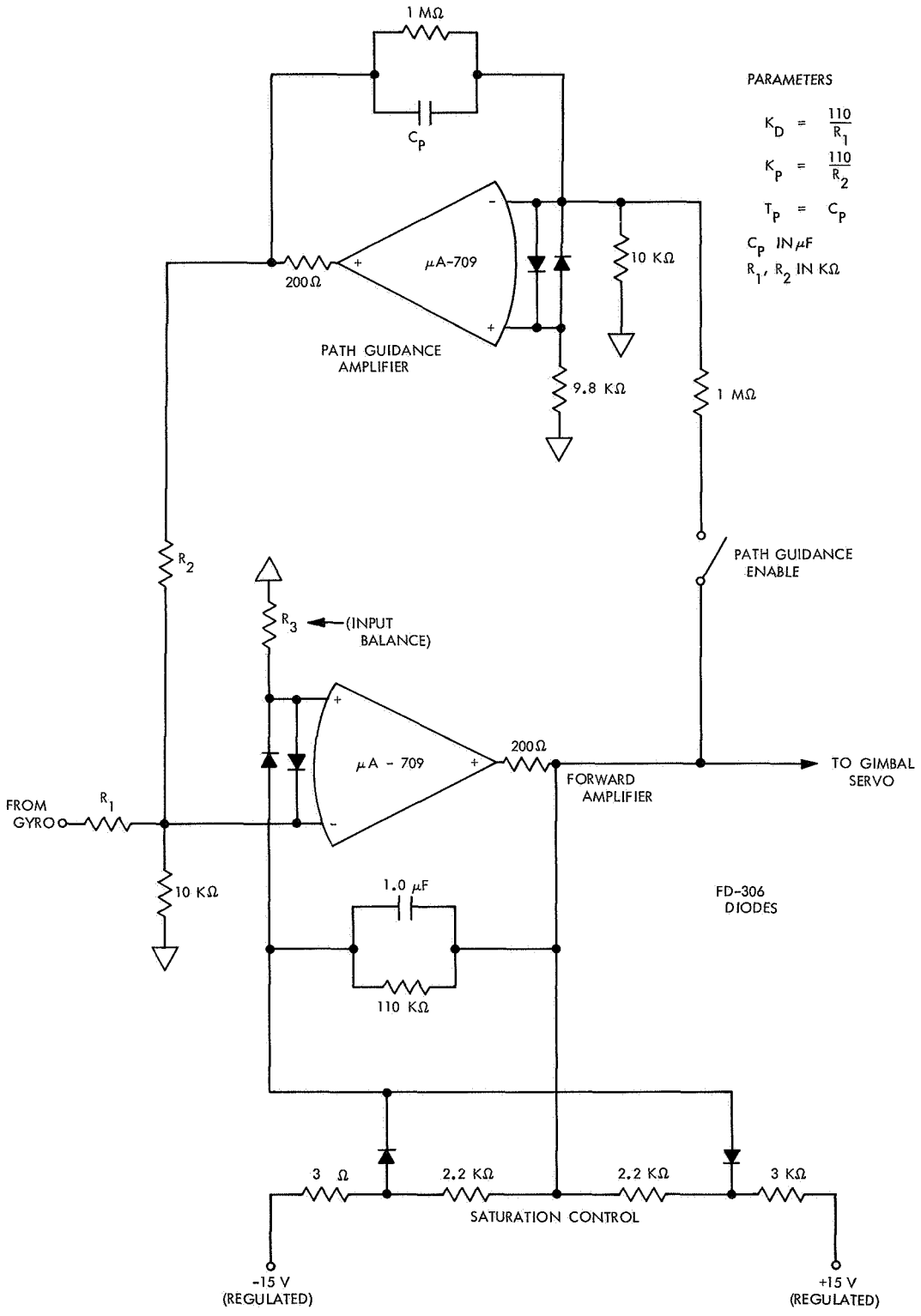

Fig. A-1. Autopilot mechanization

Appendix B

Gimbal Angle Equations

I. Relation Between Gimbal Angle and Actuator Displacement

The engine and gimbal system is shown in Fig. B-1. If the base length of the actuator is given as L and its extension, or retraction, from the base length is δ, then the gimbal angle ϕ is

$$\phi = \tan^{-1}\left(\frac{\ell}{L}\right) + \sin^{-1}\left(\frac{-\ell^2 + L\,\delta + \frac{\delta^2}{2}}{\ell\,(L^2 + \ell^2)^{1/2}}\right)$$

where ℓ is the distance from the gimbal-pivot point to the clevis plane. For the RS-1401 engine, the values are

$$L = 6.25 \text{ in.}$$

$$\ell = 2.54 \text{ in.}$$

Thus,

$$\phi = 22.116825 + \sin^{-1}\left(\frac{\frac{\delta^2}{2} + 6.25\,\delta - 6.4516}{17.1358912}\right) \text{deg}$$

The linear approximation used throughout this report was

$$\phi = \frac{180\,\delta}{\pi\,\ell}$$

It is important to assess the accuracy of this equation. At an actuator extension of 0.4433 in., the linear relation gives a gimbal angle of 10 deg where the more accurate equation yields 10.049 deg. Thus, the linear approximation is valid to engineering accuracy.

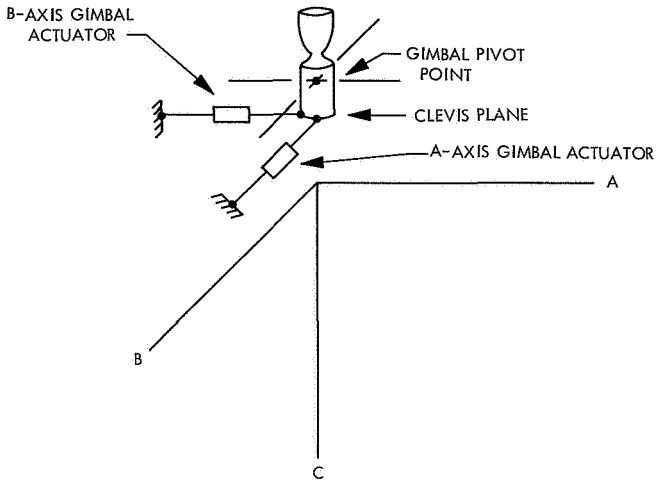

Fig. B-1. *Mariner* orbiter gimballed engine configuration

II. Gimbal-Angle Cross Coupling

When the A axis gimbal actuator extends or retracts, it causes the B axis actuator to pivot and produce a B axis error. This equivalent retraction of the B axis actuator gives rise to the angular deflection

$$\phi = \frac{-\delta_A^2}{L\,\ell}$$

For an extension of 0.4433 in., this is 0.7 deg.

Appendix C

Autopilot Pre-Aim Function

I. Description of the Pre-Aim Function

If only one fuel and one oxidizer tank are used on the *Mariner* orbiter, there exists the possibility of a large transverse CG shift. This is because there is a 1.6:1 mass differential between oxidizer and fuel. This CG shift is predictable as a function of engine burn time and, thus, can be compensated by pre-aiming the engine with a bias of the gimbal servo null by a digital command from the CC&S. The engine and gimbal system would be maintained so that the engine without bias would point through the calculated CG position when the spacecraft is in midcourse correction configuration. For the first midcourse, second midcourse, and orbit insertion no pre-aim is required, and the CC&S would command a null shift of zero. During the long orbit-insertion burn, the major CG shift would occur. This could represent a gimbal angle motion of 4 deg; however, this motion would be slow and hence easily tracked by the autopilot system. Path guidance will provide automatic attitude compensation. For subsequent in-orbit burns the CC&S will send a digital word to the pre-aim system which will point the engine at the calculated CG location for the orbit configuration.

II. Pre-Aim Mechanization

A typical pre-aim circuit is shown in Fig. C-1. At the start of a maneuver sequence (event M-1), the CC&S will send a signal, in digital form, representing the amount of pre-aim. This word will be clocked into the shift register which will operate semiconductor switches gating a reference supply voltage into a ladder network. The ladder network output will pass through isolation and d-c restoring amplifiers to become the pre-aim analog voltage. This voltage will then be fed into the summing junction of the gimbal servo and provide the pre-aim of the engine.

III. Pre-Aim Circuit Accuracy

An important question to be resolved is how many bits are necessary in the digital-to-analog converter. The accuracy of the pre-aim analog voltage must be commensurate with the resolution of the gimbal servo. Starting with the gimbal position transducer, the basic linearity is ½% or 0.003 in. Along with this is the accuracy of the ac supply to the transducer which is assumed to be ½% or 0.001 in. at the equivalent of 4.5-deg gimbal angle. The inherent

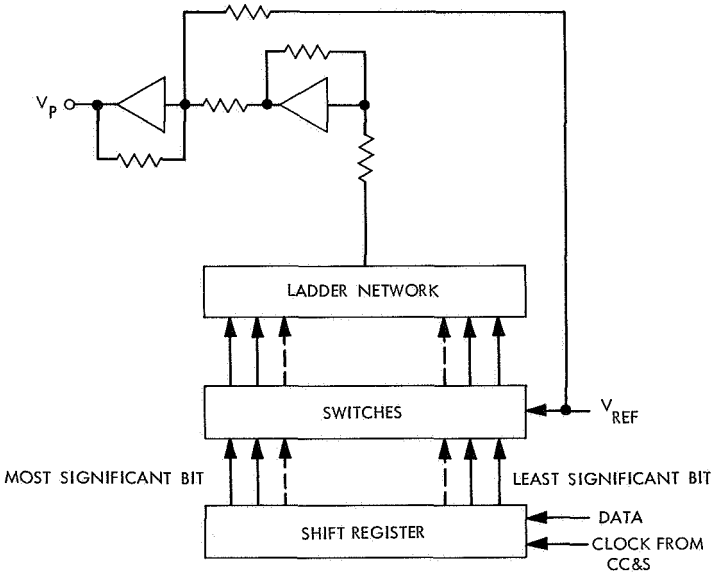

Fig. C-1. Pre-aim voltage generation

backlash is 0.002 in. and the gimbal-servo summing junction accuracy is assumed to contribute another 0.002 in. if a 10^5-gain-class amplifier is used with ½% resistors. Finally, the major resolution limit is the threshold of the motor under load. If a voltage at the armature of 16.5 V is necessary to start the gimbal moving, and the loop gain is set at 7000 armature V/rad of gimbal angle, then this contribution is 0.006 in. The worst-case total is 0.014 in. or the equivalent of 0.315 deg.

Assuming the pre-aim circuit is set for the range of +5 to −1 deg, a 7-bit register would have a scale factor of 0.0472 deg/bit, which is 6 times the gimbal servo resolution. When the other pre-aim circuit error sources are considered, the 7-bit shift register appears to be well suited for this task.

IV. Commanded Turn Considerations

The commanded turns must be biased to account for the pre-aim angle. For example, assume the pre-aim was set at 4 deg and the actual CG shift was equivalent to only 3 deg. The commanded turns made on the basis of 4 deg will still be correct, however, because path guidance will automatically rotate the spacecraft in the inertial frame to provide the added degree.

Appendix D

Autopilot Mixing

With the two-tank configuration discussed in Appendix C, it is almost certain that the tanks will not be placed with their centers along a spacecraft coordinate system axis. Consider a configuration as shown in Fig. D-1. The engine system is set so that the pre-aim is accomplished by biasing only one gimbal actuator, in this example the A-axis actuator. These engine coordinates are produced by performing an Euler rotation θ about the spacecraft roll axis and, thus, the transformation from spacecraft to engine coordinates is given by

$$A = \begin{bmatrix} \cos\theta & \sin\theta & 0 \\ -\sin\theta & \cos\theta & 0 \\ 0 & 0 & 1 \end{bmatrix}$$

For the example under consideration, $\theta = -135$ deg.

The major importance of the A, B, C system is the fact that the inertia matrix for this system will have small off-diagonal terms. Due to the large quantity of fuel, the XY product of inertia for the spacecraft coordinate system may be large enough to degrade a control system designed on the basis of three single-axis systems, such as presented in this report. A simple method for circumventing this problem is to design the autopilot system to control about the A, B, C system. Let I be the inertia matrix for the A, B, C system and, as before, let I represent the X, Y, Z system inertia. I is given by the similarity transform of I

$$\hat{I} = A\, I\, A^T$$

The outputs of the gyros can be mixed at the autopilot inputs to produce signals representing gyros located on the A, B, C axes. With this in mind, the procedure for design will be to proceed as indicated in this report but use $\hat{I}$ instead of I for the inertia tensor. In this procedure, the gain is determined for both autopilot channels (Fig. 33). These two gains are interpreted as A and B axis gains, and are synthesized from pitch and yaw gyro outputs, as follows:

Assume V_X and V_Y from the real gyros are mixed to produce the A and B equivalents V_A and V_B. Then

$$V_A = V_X \cos\theta + V_Y \sin\theta$$
$$V_B = -V_X \sin\theta + V_Y \cos\theta$$

Knowing K_{DA} and K_{DB}, the gyro-to-autopilot gains can be computed (Fig. D-2)

$$V_1 = K_{DA}\, V_A = (K_{DA} \cos\theta)\, V_X + (K_{DA} \sin\theta)\, V_Y$$
$$V_2 = K_{DB}\, V_B = (-K_{DB} \sin\theta)\, V_X + (K_{DB} \cos\theta)\, V_Y$$

Identifying terms,

$$K_{XA} = +K_{DA} \cos\theta$$
$$K_{XB} = -K_{DB} \sin\theta$$
$$K_{YA} = +K_{DA} \sin\theta$$
$$K_{YB} = +K_{DB} \cos\theta$$

For the $\theta = -135$ deg case the autopilot could be realized using the circuit in Fig. D-3.

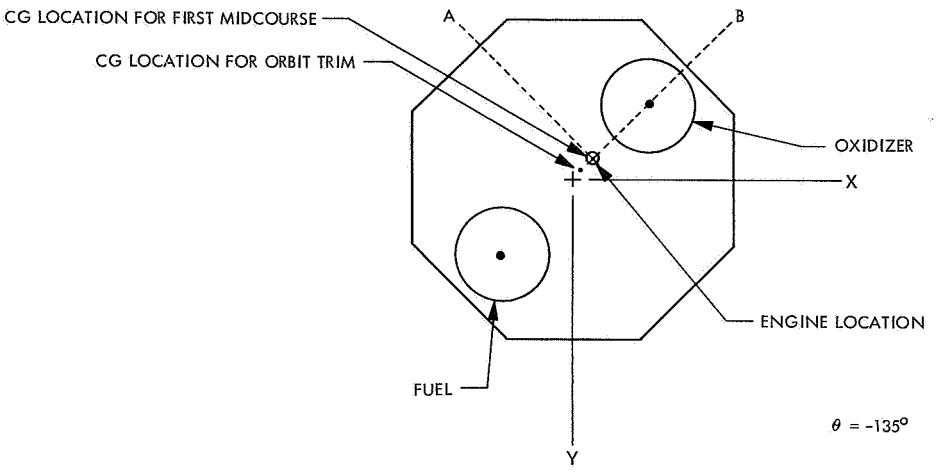

Fig. D-1. Typical two-tank *Mariner* orbiter configuration

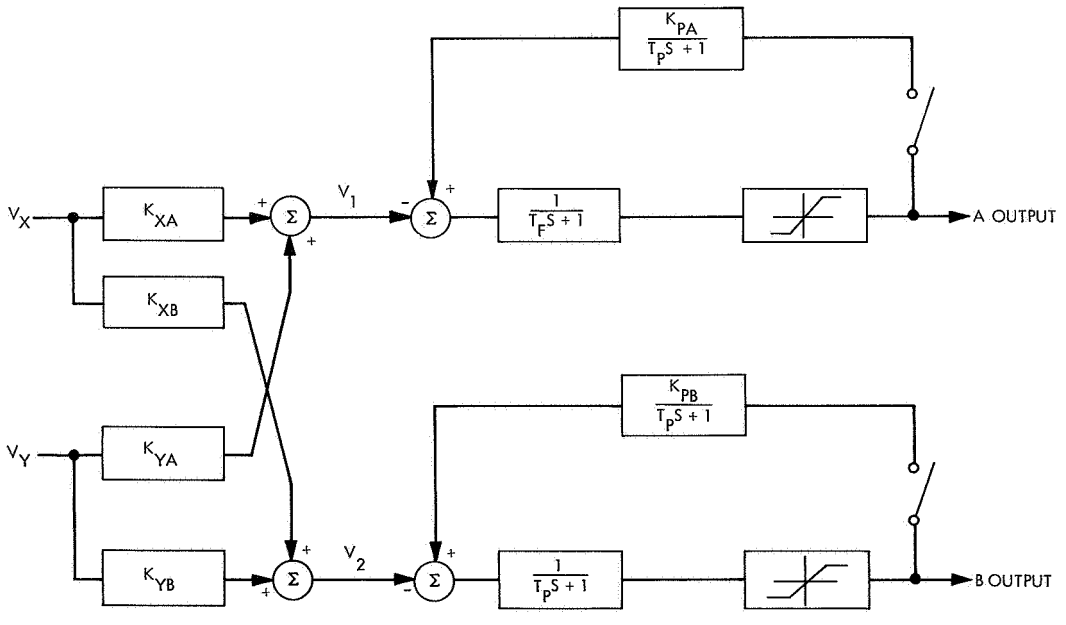

Fig. D-2. Mixing autopilot

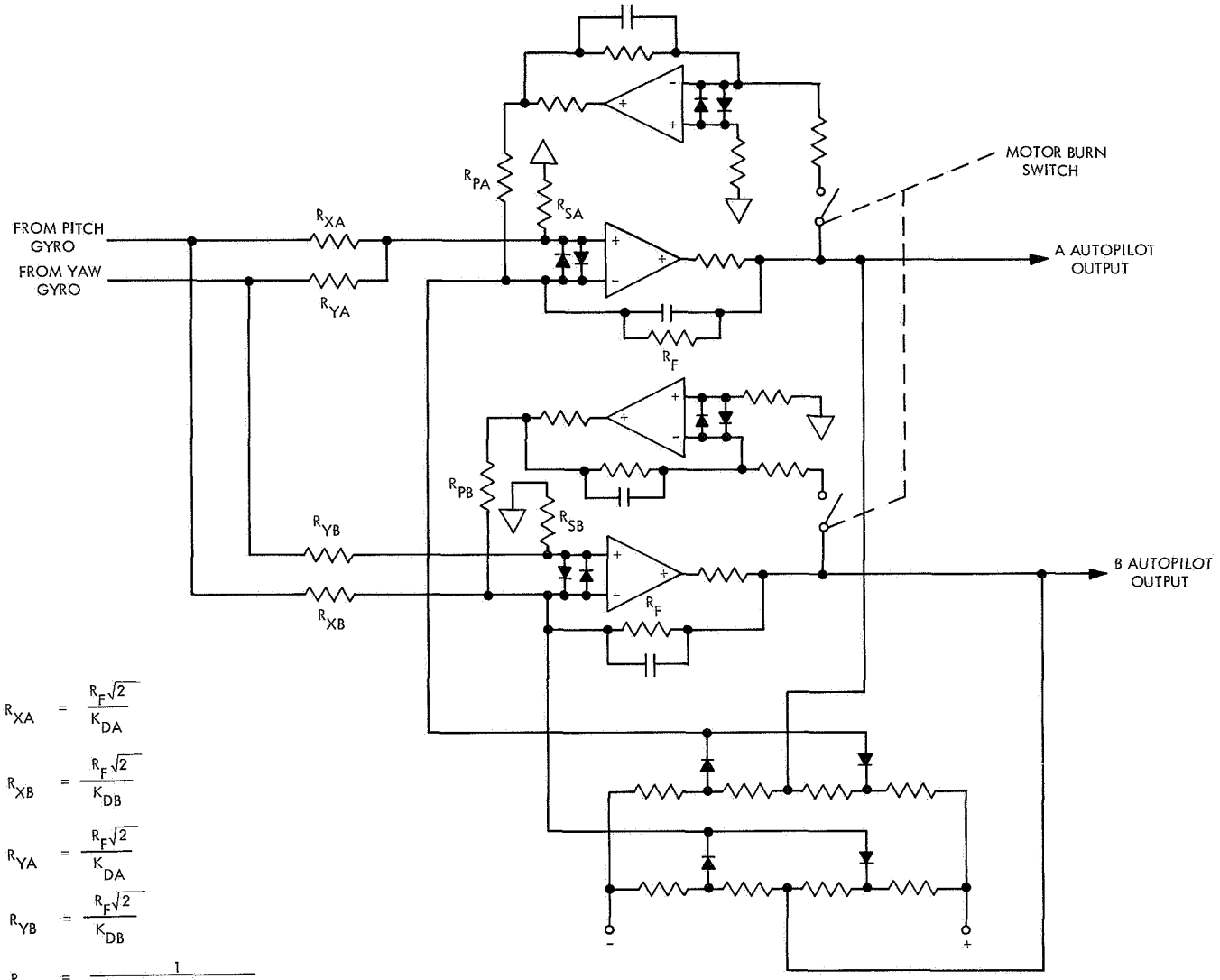

$$R_{XA} = \frac{R_F\sqrt{2}}{K_{DA}}$$

$$R_{XB} = \frac{R_F\sqrt{2}}{K_{DB}}$$

$$R_{YA} = \frac{R_F\sqrt{2}}{K_{DA}}$$

$$R_{YB} = \frac{R_F\sqrt{2}}{K_{DB}}$$

$$R_{SA} = \frac{1}{\frac{1}{R_{YA}} + \frac{1}{R_{PA}} + \frac{1}{R_F} - \frac{1}{R_{XA}}}$$

$$R_{SB} = \frac{1}{-\frac{1}{R_{YB}} + \frac{1}{R_{PB}} + \frac{1}{R_F} + \frac{1}{R_{XB}}}$$

Fig. D-3. *Mariner* orbiter autopilots with mixing for $\theta = -135$ deg

Appendix E

Autopilot System Using an Active Integrator

It appears that it may be feasible to use active electronic integration in conjunction with the *Mariner* orbiter gyros. This means that the high-gain gyros will be operated exclusively in the rate mode, and that position information will be obtained by integration using one of the newly developed temperature-stabilized IC amplifier systems. If this is done, the gyro system will have separate rate and position outputs which will have to be mixed in the autopilot circuits. Consideration of a two-tank configuration is provided in Appendixes C and D. The gyro/autopilot interface for this situation is shown in Fig. E-1. To determine the mixing gains, the basic procedure described in this report is used. Note where loop gain is determined; here the procedure is interrupted, and K_D is not solved for. Instead, compute

$$K_G K_D = \frac{K I}{K_A T d_1}$$

for both the A and the B axes. Now let

τ = desired gyro rate to position time constant

θ = engine Euler angle (rad)

K_T = gyro torquer scale factor (deg/h/mA)

R = total series torquer resistance

K_I = integrator gain

Then

$$K_{RXA} = \frac{\tau K_T}{206265R}\left(K_g K_D\big|_{A_{\text{axis}}}\right)\cos\theta$$

$$K_{PXA} = \frac{K_T}{206265RK_I}\left(K_g K_D\big|_{A_{\text{axis}}}\right)\cos\theta$$

$$K_{RYA} = \frac{\tau K_T}{206265R}\left(K_g K_D\big|_{A_{\text{axis}}}\right)\sin\theta$$

$$K_{PYA} = \frac{K_T}{206265RK_I}\left(K_g K_D\big|_{A_{\text{axis}}}\right)\sin\theta$$

$$K_{RXB} = \frac{-\tau K_T}{206265R}\left(K_g K_D\big|_{B_{\text{axis}}}\right)\sin\theta$$

$$K_{PXB} = \frac{K_T}{206265RK_I}\left(K_g K_D\big|_{B_{\text{axis}}}\right)\sin\theta$$

$$K_{RYB} = \frac{\tau K_T}{206265R}\left(K_g K_D\big|_{B_{\text{axis}}}\right)\cos\theta$$

$$K_{PYB} = \frac{K_T}{206265RK_I}\left(K_g K_D\big|_{B_{\text{axis}}}\right)\cos\theta$$

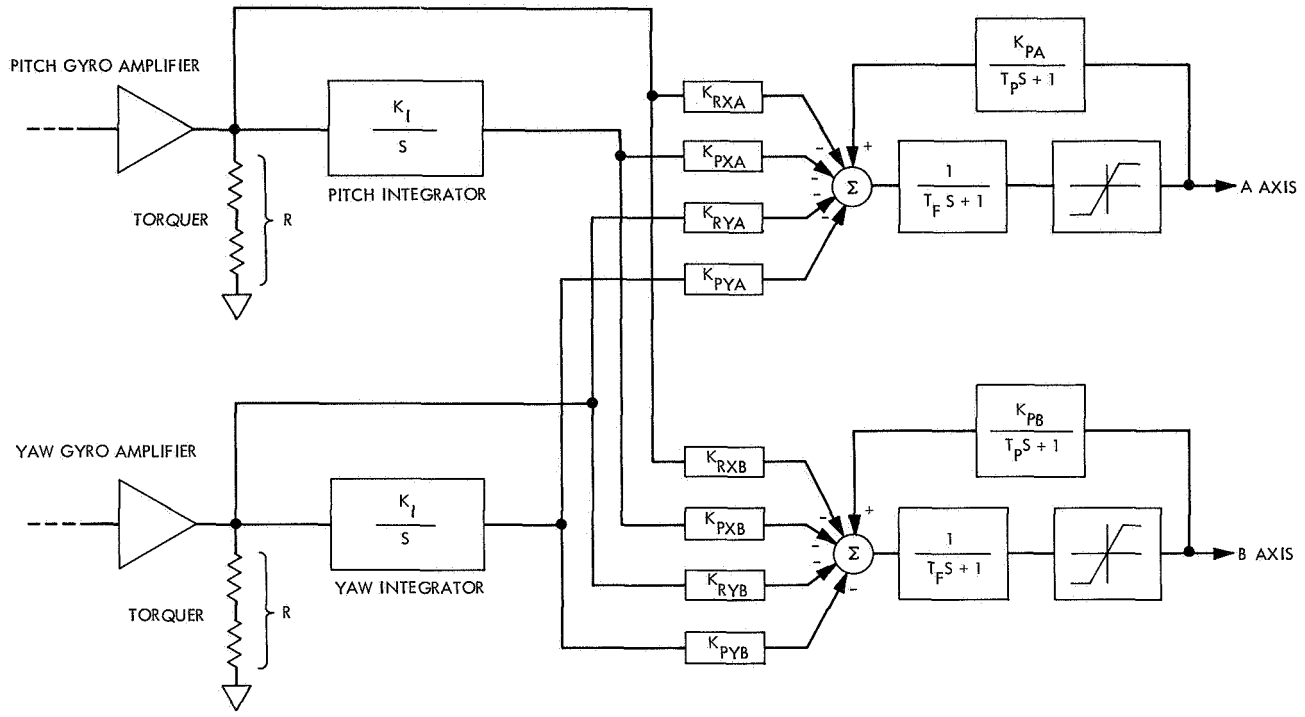

Fig. E-1. Gyro/autopilot interconnection for the electronic integrator

Appendix F

Engine Gimbal Reaction Torque

When the gimbal actuators operate, there is a reaction torque felt by the spacecraft. Since the actuators do not back-drive easily, the motion of the spacecraft essentially has no effect upon the gimbal angle. Thus, gimbal angles are treated dynamically as holonomic constraints and these angles are then functions of time determined only by the gimbal servos

$$\phi_X = f_X(t)$$

$$\phi_Y = f_Y(t)$$

and $[\phi_X - f_X(t)]$ and $[\phi_Y - f_Y(t)]$ are adjoined to the system through Lagrange multipliers. However, when the system is simplified to a single-axis, small-angle problem, the equation set becomes trivial and the reaction torque on the spacecraft is seen to be

$$N = -(I_E + M_E \ell \mathbf{r}) \ddot{\phi}$$

where

I_E = engine and gimbal moment of inertia

M_E = engine mass

ℓ = distance from the CG to the center of mass of the engine

$\mathbf{r}$ = distance in the direction of the exhaust of the center of mass of the engine from the gimbal pivot point

As shown in Fig. 34, the engine reaction torque requires an additional block from $\ddot{\phi}$ to pitch torque. In Fig. 34,

$$N_{\text{PITCH}} = -Td_1 \phi_X$$

and this is now modified to

$$N_{\text{PITCH}} = -[(I_E + M_E \ell \mathbf{r}) S^2 + Td_1] \phi_X$$

Substituting values for the RS-1401 engine gives rise to real zeros at ± 100. Obviously, these will have a negligible effect on the system.